UNIVERSITY OF OKLAHOMA
GRADUATE COLLEGE

MECHANISTIC MODEL OF COMPLEX CONDUCTIVITY OF POROUS MEDIA CONTAINING CONDUCTIVE PARTICLES OF VARYING WETTABILITY

A THESIS
SUBMITTED TO THE GRADUATE FACULTY
in partial fulfillment of the requirements for the
Degree of
MASTER OF SCIENCE

By

YUTENG JIN
Norman, Oklahoma
2019

MECHANISTIC MODEL OF COMPLEX CONDUCTIVITY OF POROUS MEDIA CONTAINING CONDUCTIVE PARTICLES OF VARYING WETTABILITY

A THESIS APPROVED FOR THE
MEWBOURNE SCHOOL OF PETROLEUM AND GEOLOGICAL ENGINEERING

BY

Dr. Siddharth Misra, Chair

Dr. Chandra S. Rai

Dr. Ali Tinni

Abstract

Electrically conductive particles, such as graphite and pyrite particles, and surface-charge-bearing nonconductive particles, such as sand and clay grains, are commonly present in subsurface geological formations. When a fluid-filled porous geomaterial is exposed to an external electromagnetic (EM) field generated by electromagnetic measurement tool, the constituent conductive and non-conductive particles surrounded by in situ brine give rise to interfacial polarization (IFP) effects, which cause frequency dispersions of effective conductivity and effective permittivity of the fluid-filled porous geomaterials. IFP effects when neglected lead to inaccurate interpretation of electromagnetic logs/measurements, especially in clay-, graphite- and pyrite- rich formations. Also, there is no mechanistic model that accounts for the effect of wettability of conductive particles and surface-charge-bearing particles on the electromagnetic logs/measurements of geomaterials.

This thesis describes a mechanistic model (namely PS model) that couple surface-conductance-assisted interfacial polarization (SCAIP) model with perfectly polarized interfacial polarization (PPIP) model to estimate effective conductivity and effective permittivity of shale formations containing both nonconductive and conductive particles at various fluids saturations. The model is developed based on the Poisson-Nernst-Planck (PNP) equations for a dilute solution in a weak electrical field regime to calculate the dipolarizability of the representative volume comprising a single isolated spherical particle in an electrolyte host. Then the effective medium theory is used to determine effective complex conductivity of the whole mixture. The PS model is further improved to consider the wettability effect by introducing a wettability model, which is developed based on the solution of the Young-Laplace equation that determines the shape of the oil-water interface (meniscus) at equilibrium.

The model shows that the IFP effects of conductive particles dominate the frequency dispersions of complex conductivity as compared to nonconductive particles. Also, the frequency dispersion reduces as contact angle or oil saturation increases, and the effect of oil saturation on the frequency dispersions of complex conductivity is less than the effect of contact angle (i.e. the contact angle plays a primary effect and oil saturation plays a secondary effect). At the end of this thesis, a Markov chain Monte Carlo (MCMC) inversion method is coupled with the PS model to process the multifrequency electromagnetic logs/measurements to estimate oil saturation, contact angle and conductivity of brine.

Dedication

To my dear mom and dad, for their countless love and support.

Acknowledgements

First and foremost, I would like to express my sincerest thanks to my supervisor, Dr. Siddharth Misra, for his supervision and financial support during my research as a master's student. He offered me a lot of valuable suggestions on the research, including creatively thinking, problem solving and professional paper writing. Under his support and guidance, I learnt to be a professional researcher.

I would like to thank my committee members, Dr. Chandra S. Rai and Dr. Ali Tinni, for taking time to reviewing this work and making valuable comments.

I would like to thank Schlumberger Limited for supporting this research project and providing valuable technical suggestions. I'd like to thank Dr. Dean Homan, Research Scientist at Schlumberger, who provided great help in the conceptualization and start of this project. I'd like to thank Dr. Denis Heliot, Global Interpretation Métier Manager at Schlumberger, for his support that was very valuable during the initial stages of the project. I'd like to thank Joe Zapf, Development Technician at Schlumberger, for handling logistics that streamlined the execution of this project. Also, I'd like to thank Dr. Chang-Tu Hou, Senior Scientist at Schlumberger-Doll Research Center, for valuable technical suggestions and for reviewing this work.

Finally, I would like to express my appreciation and deepest love to my parents and family for their constant support—both emotional and financial—over the years, so that I can focus on my research during my time at OU.

Table of Contents

List of Figures and Tables

List of Figures

List of Tables

Nomenclature

Acronyms

EM = electromagnetic
IFP = interfacial polarization
PDE = partial differential equations
PNP = Poisson-Nernst-Planck
PPIP = perfectly polarized interfacial polarization
PS = PPIP-SCAIP
SCAIP = surface-conductance-assisted interfacial polarization

Symbols

a = characteristic length of inclusion phase (m)
A_o = surface area of graphite particle covered by oil (m^2)
A_s = surface area of graphite particle (m^2)
A_w = surface area of graphite particle covered by water (m^2)
B_o = Bond number
c = charge density variation (1/m^3)
d = net charge density variation (1/m^3)
D = diffusion coefficient of charge carriers (m^2/s)
Δ (∇^2) = Laplace's operator
e = Euler's number
$\boldsymbol{e}$ = electric field vector
E_0 = amplitude of the electric field (V)
ε = dielectric permittivity (F/m)
ε_0 = vacuum permittivity (8.854×10^{-12} F/m)
ε_{eff} = effective dielectric permittivity of the mixture (F/m)
ε_r = relative permittivity
f = frequency (Hz)
$f(\omega)$ = dipolarizability (dipolar field coefficient)
$f(\varphi)$ = a function of wetting angle φ
g = gravitational acceleration (N/kg)
G = dimensionless form of $h - h_i$
$h(r)$ = height of oil-water interface at any distance r away from the vertical axis z (m)
$\hat{h}$ = dimensionless form of h
h_c = height where the oil-water interface contacts the particle surface (m)
h_i = height of oil-water interface in the absence of wetting of graphite (far-field height) (m)
H = mean curvature of the meniscus surface (m^{-1})
i = square root of -1
i_n = modified spherical Bessel function of the first kind of nth order
I_n = modified Bessel function of the first kind of nth order
$\boldsymbol{j}$ = current density (A/m^3)
k_B = Boltzmann's constant
k_n = modified spherical Bessel function of the second kind of nth order

K_n = modified Bessel function of the second kind of nth order
L_c = capillary length (m)
λ = surface conductance (S)
λ_D = Debye screening length (m)
μ = electrical mobility [$\mathrm{m^2/(V\cdot s)}$]
n = an integer referring to the order of the standing wave solution
N = charge carrier density ($1/\mathrm{m}^3$)
ω = angular frequency of the electric field (rad/s)
Δp = Laplace pressure (Pa)
p_o = proportion of graphite surface that covered by oil (%)
p_w = proportion of graphite surface that covered by water (%)
P_f = net free charge density ($\mathrm{C/m^3}$)
P_n^0 = associated Legendre functions of the first kind of nth order
φ = electrical potential (in PS model) (V)
φ = wetting angle (in wettability model) (°)
ϕ = porosity of the porous media (%)
ϕ_j = volume fraction of medium j in the mixture (%)
ϕ_o = volume fraction of oil in the mixture (%)
ψ = angle between oil-water interface and the horizon (x-axis) at contact point (°)
q = elementary charge (1.6×10^{-19} C)
Q_n^0 = associated Legendre functions of the second kind of nth order
r = radial distance along the normal to the interface (in PS model) (m)
r = distance from vertical axis z (in wettability model) (m)
$\hat{r}$ = dimensionless form of r
R = radius of graphite particle (m)
ρ_o = density of oil ($\mathrm{kg/m^3}$)
ρ_w = density of water ($\mathrm{kg/m^3}$)
ρ = surface charge density ($\mathrm{C/m^2}$)
s = total ion density variation ($1/\mathrm{m}^3$)
S_o = oil saturation (%)
σ_j = electrical conductivity of medium j (S/m)
σ = interfacial tension between oil and water (N/m)
σ^* = complex electrical conductivity (S/m)
σ_{eff} = effective electrical conductivity of the mixture (S/m)
σ_{eff}^* = effective complex electrical conductivity of the mixture (S/m)
t = time (s)
T = absolute temperature (K)
θ = angle between normal to the interface and incident external electric field (in PS model) (°)
θ = contact angle (in wettability model) (°)
Z = charge number

Subscripts

0 = at time equal to 0 s
c = clay

$cond$ = conductive particles
eff = effective
g = graphite
go = graphite surrounded by oil
gw = graphite surrounded by water
h = host medium
i = inclusion phase
j = type of medium/phase
n = an integer referring to the order
$\hat{n}$ = unit vector
$ncond$ = nonconductive particles
o = oil
p = pyrite
r = relative
s = sand

Superscripts

+ = positively charged carrier
- = negatively charged carrier

Chapter 1: Introduction

This thesis presents work performed for a Master of Science in Petroleum Engineering degree that was conducted at the Mewbourne School of Petroleum and Geological Engineering of the University of Oklahoma. The research presented the development of a mechanistic model of multi-frequency complex conductivity of porous media containing water-wet nonconductive particles and conductive particles of varying wettability. The research work was done in close collaboration and supervision of Dr. Siddharth Misra.

1.1. Motivation and Problem Statement

Under an external electric field generated by electromagnetic (EM) measurement tool, conductive and surface-charge-bearing nonconductive particles in the formation give rise to interfacial polarization (IFP) effects, which causes frequency dispersion of effective conductivity and effective permittivity of the mixture containing such particles. The neglect of IFP effects leads to inaccurate estimation of petrophysical properties of formations, especially in clay- and pyrite-rich formations. Also, the wettability of conductive particles and surface-charge-bearing particles influences the electromagnetic properties of subsurface formations or the rock samples brought to the surface. A mechanistic model is needed to couple the interfacial polarization of uniformly distributed water-wet nonconductive spherical grains possessing surface conductance with interfacial polarization of uniformly distributed conductive spherical inclusions in redox-inactive conditions of varying wettability.

1.2. Objective

a. Develop a mechanistic model that accounts for the interfacial polarization effects of conductive particles and surface-charge-bearing nonconductive particles on the multifrequency electromagnetic logs/measurements.
b. Develop a mechanistic model that accounts for the effect of wettability of conductive particles on the multifrequency electromagnetic logs/measurements.

1.3. Thesis Structure

Chapter 1 is the introduction about this thesis.

Chapter 2 contains a literature review about interfacial polarization phenomena and wettability effect.

Chapter 3 discusses a detailed derivation of the mechanistic model that accounts for the interfacial polarization effect of conductive and surface-charge-bearing nonconductive particles on electromagnetic logs (PS model) and the derivation of the mechanistic model that accounts for wettability effect (wettability model).

Chapter 4 shows the validation of the PS model.

Chapter 5 presents some results and discussions about the models.

Chapter 6 discusses the application of MCMC inversion method to estimate model parameters (oil saturation and contact angle) by processing the multi-frequency electromagnetic logs.

Chapter 7 is the conclusion

Chapter 2: Literature Review

2.1. Interfacial Polarization Effect

Interfacial polarization phenomena (Dukhin et al., 1974; Wong, 1979; Schmuck and Bazant, 2015) influences the migration, accumulation, depletion, and diffusion of charge carriers. If neglected, interfacial polarization (IFP) effects will lead to inaccuracy when estimating petrophysical properties of formations using conventional resistivity/conductivity/permittivity interpretation methods (Clavier et al., 1976; Misra et al., 2016a). Some of the interpretation techniques for the subsurface galvanic resistivity (laterolog), electromagnetic (EM) induction and EM dielectric dispersion logs do not consider the IFP effects (Anderson et al., 2007; Corley et al., 2010), which cause inaccurate estimates for pyrite-rich sedimentary rocks (Altman et al., 2008) and pyrite- and graphite-rich organic source rocks (Altman et al., 2008). Although in the last decade, some papers included IFP effect in EM induction logs (MacLennan et al., 2013), or in dielectric model which considers cation exchange capacity (Revil, 2013), there is still a need to investigate the IFP effect. Recently, for hydrocarbon volume estimation, Deng et al. (2018) applied spectral induced polarization method to estimate oil saturation in oil-contaminated clayey soils. Freed et al. (2018) also developed a physics-based model for the dielectric response that accounts for the IFP effect due to the cation exchange capacity in low-salinity shaly sands formations.

Mechanistic model of the IFP phenomena can improve resistivity/conductivity/permittivity interpretation in clay- and conductive-mineral-rich formations. To model the IFP effect of electrically conductive inclusions, Misra et al. (2016b) applied Poisson-Nernst-Planck (PNP) equation. Their model predictions have a good match with laboratory measurements on conductive-mineral-bearing mixtures. Moreover, several mathematical models have been developed in the fields of petrology (Revil et al., 2017), geophysics (Revil, 2012; Placencia-Gómez and Slater, 2014), biology (Grosse and Schwan, 1992; Zheng and Wei, 2011), electrochemistry (Chu and Bazant, 2006) and colloidal science (Grosse and Barchini, 1992; Grosse et al., 1998), all of which facilitate the study of interfacial polarization effects arising from various mechanisms. In order to accurately interpret multi-frequency electromagnetic measurements, IFP phenomena around conductive and non-conductive particles should be accounted for. The influence of wettability of conductive particles on the IFP phenomena should also be considered.

2.1.1. Interfacial polarization around surface-charge-bearing nonconductive particles

Various mixing models have been developed to quantify the effects of various interfacial polarization phenomena. The model proposed by Schwarz (1962) considers interfacial polarization (IFP) effect around charged nonconductive particles. It assumes a diffusion of counterion layer moving along the surface of the charged particle by calculating the potential outside the counterion layer as a solution of Laplace's equation rather than Poisson's equation. However, this model fails to account for all the bulk diffusion effects. In contrast, Dukhin et al. (1974) concluded that the mechanism behind interfacial polarization is the diffusion of ions in the bulk electrolyte around the particle. They were unable to provide analytical expressions for IFP effects in terms of various relaxation parameters due to mathematical complexity caused by non-linearity of Dukhin et al. (1974) equation. This model, called the standard model in colloidal chemistry, does not consider the existence of a Stern layer with mobile ions. Grosse and Foster (1987) developed an analytical solution of IFP effect by developing a simplified model of charged nonconductive spherical particles in bulk electrolyte. In their model, positive ions from the bulk electrolyte can freely exchange with the positively charged counterion layer while the negative ions are excluded from the counterion layer. This model was generalized in Grosse (1988) by allowing arbitrary charge in nonsymmetric electrolytes, assuming finite surface conductivity and considering the entire frequency spectrum.

2.1.2. Interfacial polarization around conductive particles

Garcia et al. (1985) developed a model for conductive spherical particles with insulating shells (for e.g. oxidized surface of pyrite) in a conductive medium where the diffusive effects play an important role. Grosse and Barchini (1992) improved the previous theory for infinitely conductive spherical particles in bulk electrolyte by considering ion flow across the interface. Moreover, in comparison to dielectric mixture formulas, Tuncer et al. (2001) applied a finite element method on cylinder-like conductive inclusion phase to investigate the dielectric relaxation phenomena. Their result shows the two methods match well at low inclusion concentrations. However, as the concentration of inclusion increases, mutual interaction of the inclusions becomes significant. Recently, Misra et al. (2016b) developed a perfectly polarized interfacial polarization (PPIP) model to investigate interfacial polarization phenomena around conductive particles. Their work involves solving the Poisson-Nernst-Planck (PNP) equations and applying effective medium theory. The model is successfully validated using published experimental data (Misra et al., 2016a).

2.2. Wettability Effect

Kerogen, which is found to be commonly present in mudrock, is believed to be the precursor of graphite (Ujiié, 1978). Buried under deep ground, kerogen matures through diagenesis, catagenesis and metagenesis processes with the increase of temperature and pressure. Once kerogen maturation reaches beyond the metagenesis stage, graphitization would occur (Spötl et al., 1998), where the structure of kerogen undergoes further progressive rearrangements toward forming ordered carbon structure and increasing aromatization, which allows for neat molecular stacking in sheets. The final stable structure reached under high pressure and temperature is graphite (Tissot and Welte, 2012). Thus, graphite can be found in hydrocarbon-bearing rocks, sedimentary rocks and shales (Winchell, 1911; Clark, 1921; Bustin et al., 1995).

Wettability is defined as the tendency of one fluid to spread on, or adhere to, a solid surface in the presence of other immiscible fluids (Crain, 2002). The wettability of graphite is of interest to academics. Chakarov et al. (1995) mentioned that water can adsorb on the graphite surface by forming hydrogen-bonded aggregates. As discussed by Kozbial et al. (2014), highly ordered pyrolytic graphite (HOPG) is intrinsically water wet, proved by measuring the water contact angle within 10 seconds after graphite exfoliation. The author also observed the wettability of graphite gradually change to oil wet (or intermediate wet) after exposure to the ambient air, which is explained by the adsorption of hydrocarbon onto the graphite surface.

To investigate the effect of wettability on dielectric properties, Garrouch and Sharma (1994) conducted a series of experiments on brine-saturated Berea sandstone and Ottawa sand-bentonite packs. They concluded that dielectric is constant hardly affected by wettability for fully-brine-saturated rocks in absence of any conductive inclusions. Further, Capaccioli et al. (2000) investigated the wettability effect on electrical responses of partially saturated porous media by experiments. Their findings show that the change from strongly water wet to strongly oil wet will affect connectivity and shape of water phase, which lead to a smaller charge transport contribution at low frequencies and smaller dielectric strength as well as shorter characteristic times of Maxwell–Wagner–Sillars (MWS) relaxation at higher frequency. Bona et al. (2002) performed experiments to study the influence of wettability on the electrical properties of porous media. They conclude that at low frequencies, charge transport is the dominant mechanism, and the governing factor is the connectivity of the water phase. While at high frequencies, the shape factor of the water phase is the controlling parameter. In fact, wettability and electrical properties are closely related such that wettability can be estimated using the electrical properties (Bona et al., 1998; Bona et al., 1999; Moss et al., 2002; Al-Ofi et al., 2018). Additionally, Nguyen et al. (1999) observed that the dielectric permittivity of oil-wet sand is smaller than that of the water-wet sand at low water saturation, while the dielectric permittivity of oil-wet sand becomes much larger than that of the water-wet sand at higher water saturation. Revil et al. (2011) observed that both resistivity and magnitude of the phase increase with the oil saturation for sand saturated with nonwetting oil, while they both decrease with the oil saturation for sand partially saturated with wetting oil.

Chapter 3: Mechanistic Model of Interfacial Polarization Considering Wettability Effect

3.1. PS Model

The PS model is developed by Misra et al. (2016b) for the first time. In this thesis, the detailed derivation of the PS model is presented. The aim of this mechanistic model is to quantify the interfacial polarization effect of conductive and surface-charge-bearing nonconductive particles on the electromagnetic properties of the mixture at various water saturation. The PS model can be used for a mixture with < 10% conductive particles. All the particles are assumed to be spherical and only interfacial polarization effects are assumed to exist. Individual inclusion phases are assumed to be isolated with each other. The magnitude of electric field variations is less than the magnitude of intrinsic electrical properties variations. EM interactions between heterogeneities are neglected, and the size of heterogeneities is less than the wavelength of EM field.

3.1.1. Assumptions

Both the SCAIP model and PPIP model are based on the Poisson-Nernst-Planck (PNP) equations for a dilute solution in a weak electrical field regime. By applying the PNP equations, we analyze the EM response of a representative volume comprising a single, isolated nonconductive inclusion possessing surface charge or electrically conductive inclusion surrounded by an electrolyte-saturated host medium (Zheng and Wei, 2011). To simplify the model, we assume only spherical particles are present in the porous media. Also, the host, inclusion, and pore-filling fluid are assumed to have homogeneous, isotropic, and non-dispersive electrical properties. Therefore, the frequency dispersion and dielectric enhancement predicted by the SCAIP model or PPIP model solely stems from the SCAIP or PPIP phenomena around the negatively charged nonconductive or electrically conductive inclusions. We also assume all the charge carriers bear unitary charge and both host and inclusion phases bear binary, symmetric charge carriers.

3.1.2. SCAIP model

Dr. Misra derived the SCAIP model in his note and the derivation was improved by me. The completed derivation of SCAIP model is presented in this section.

The surface of a nonmetallic (nonconductive) mineral, such as clay, acquires charges if the mineral is surrounded by electrolytes due to ionic adsorption, protonation/deprotonation of the hydroxyl groups, and dissociation of other potentially active surface groups, also combinedly referred as surface complexation reactions (Leroy and Revil, 2004). In this thesis, surface-conductance-assisted interfacial polarization (SCAIP) model is developed to investigate the interfacial polarization phenomena around surface-charge-bearing spherical nonconductive particles. Figure 3.1 shows SCAIP phenomena in a representative volume of a dilute mixture of uniformly distributed surface-charge-bearing nonconductive spherical inclusions in an electrolyte-saturated host medium, where interfacial polarization is independent of the direction of the externally applied electric field due to spherical symmetry.

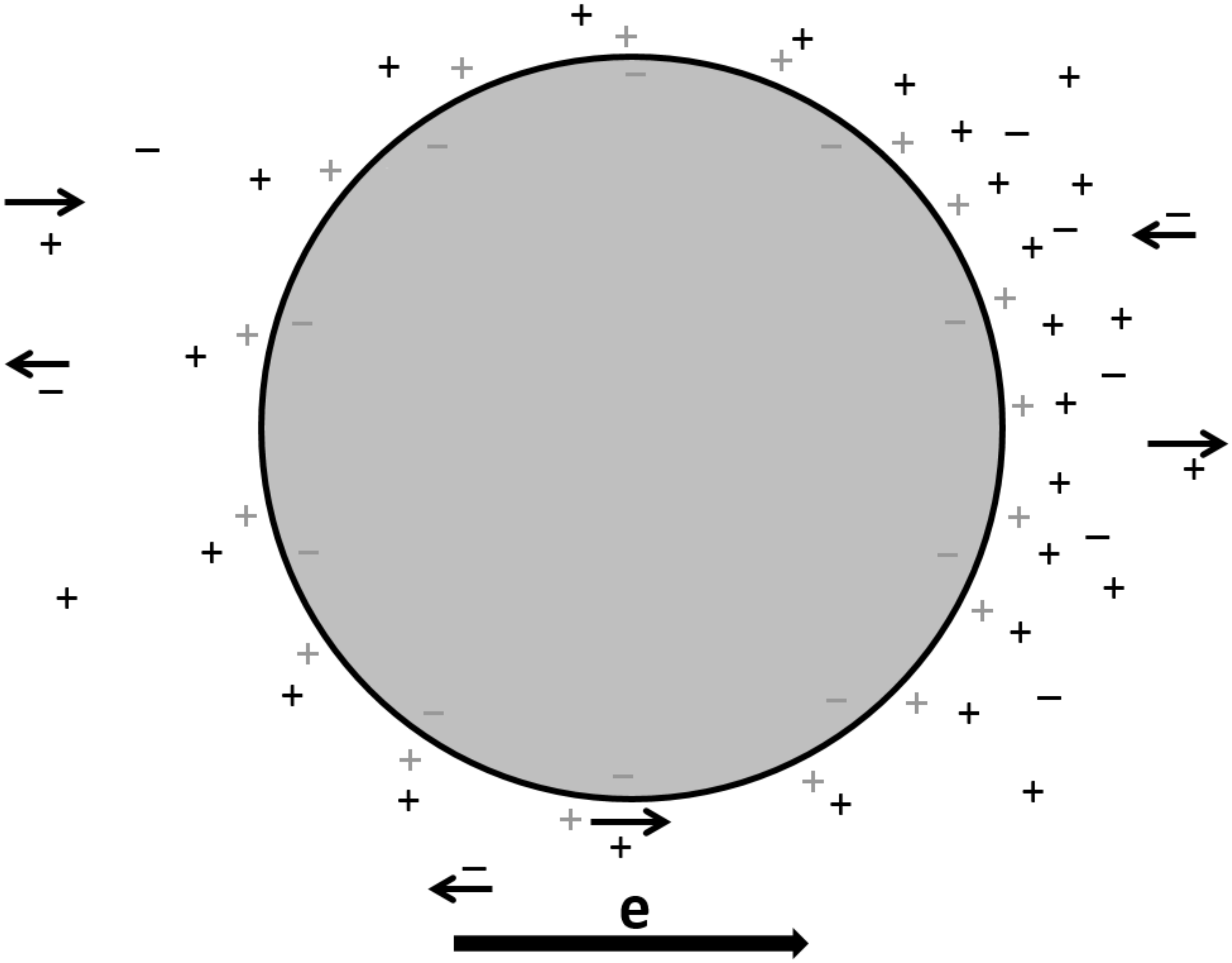

Figure 3.1. Cross-section of a nonconductive spherical inclusion possessing surface charge surrounded by an ionic host medium. The inclusion is negatively charged, surrounded by a positively charged counterion layer, which forms a Gouy-Chapman model. Charge carriers in the

ionic host medium are cations, identified by "+" symbol, and anions, identified by "-" symbol. The direction of the externally applied electrical field, **e**, is identified with a bold arrow next to the symbol "**e**". The direction of movement of the charge carriers in the ionic host medium is represented by the arrow next to the symbol of the charge carrier.

The phenomenological basis of interfacial polarization considered in our work builds on the mechanistic descriptions outlined by Grosse (1988). The negatively charged inclusion, together with its positive counterion layer, essentially behaves as a conductor of positive charge carriers, which allows the positive ions in the host medium to freely exchange with the ions in the counterion layer, and as a non-conductor of negative charges, which excludes the negative ions from the counterion layer.

In the absence of an externally applied electric field, a Gouy-Chapman double layer is assumed around the surface-charge-bearing nonconductive inclusions, where the positive counterion layer is characterized by a finite surface conductivity. We assume the thickness of counterion layer is negligible, which is valid when $a \gg \lambda_D$, where λ_D is the Debye screening length and a is the characteristic length of the inclusion phase.

3.1.2.1. SCAIP model development

The Poisson-Nernst-Planck (PNP) equation has been used to model electromigration and diffusion of ionic charge carriers in electrolytes (Zheng and Wei, 2011) and that due to holes and electrons in semiconductors (Schmuck and Bazant, 2015). It is based on a mean-field approximation of charge carrier interactions and continuum descriptions of charge concentration and electrostatic potential. We apply the PNP equations to model charge dynamics and relaxation in the representative volume containing only two phases: the host medium, denoted by subscript h, and the conductive (to be discussed in the following section) or nonconductive particles (inclusions), denoted by subscript i. In our formulation, the host medium can be assumed as a homogeneous mixture of electrolyte and nonconductive matrix or as a pure electrolyte. At time $t < 0$, it is assumed that there is no external electric field exciting the representative volume. Initial charge carrier densities at equilibrium conditions in both the host and inclusion phases are denoted as $N_{0,j}^{\pm}$, where subscript j takes the form of i for the inclusion phase and h for the host phase. Starting at time $t = 0$, the representative volume experiences a uniform externally applied electric field $E = E_0 e^{i\omega t}$, where E_0 is the amplitude of the externally applied electric field, i is square root of -1, ω is the angular frequency (rad/s) of the externally applied electric field, and e is Euler's number. Note $\omega = 2\pi f$, where f is frequency (Hz). We assume the negatively charged spherical nonconductive particle is surrounded by a layer of positively charged, conducting counterion layer, which has a surface conductance λ and bears a field-induced surface charge density $\rho e^{i\omega t} cos\,\theta$, where θ is the angle between the normal to the interface and the incident external electric field. Under a weak field approximation, charge carrier densities in host and inclusion phases are perturbed from their equilibrium conditions near the host-inclusion interfaces, resulting in a new linearly approximated charge distribution, given by

$$N_j^{\pm}(r,t,\theta) = N_{0,j}^{\pm} + c_j^{\pm}(r) e^{i\omega t} cos\,\theta \tag{1}$$

such that $\left|c_j^{\pm}\right| \leq N_{0,j}^{\pm}$, $c_j^{\pm}$ is the charge density variation near the host-inclusion interface in medium j due to the externally applied electric field and r is the radial distance along the normal to the interface. Note that in this section, for nonconductive inclusion, $c_i^{\pm}(r) = 0$. In addition, one assumption is the absence of charge carriers in the nonconductive inclusion phase, $N_{0,i}^{\pm} = 0$. Further, the symbol "+" identifies positive-charge carriers such as holes and cations, while the symbol "-" identifies negative-charge carriers such as electrons and anions.

We assume that the characteristic length a of the inclusions phase is far greater than the Debye screening length λ_D. Note that λ_D is a measure of induced charge distribution that forms around an inclusion particle due to surface charges that exist on the inclusion particle in the absence of an externally applied electric field. In other words, λ_D represents a volume outside of which surface charges on an inclusion particle are electrically screened. The characteristic length a is equal to the radius of spherical inclusion. Mathematically, $\lambda_D = \sqrt{\varepsilon_h k_B T / \left(2 Z_h^+ Z_h^- q^2 N_{0,h}\right)}$, where ε_h is dielectric permittivity of the host, k_B is Boltzmann's constant, T is absolute temperature, $Z_h^{\pm}$ is charge number of positive and negative charge carriers in the host, and q is the elementary charge. The volume fraction of conductive (for e.g. pyrite) and nonconductive particles (for e.g. clays) is assumed to be in the range of 5%-15%. Another simplifying assumption is that all the charge carriers bear unitary charge and that both host and inclusion phases bear binary, symmetric charge carriers. In other words,

$$Z_j^{\pm} = 1, \mu_h^+ = \mu_h^- = \mu_h, \mu_i^+ = \mu_i^- = \mu_i, N_{0,i}^+ = N_{0,i}^- = N_{0,i}, N_{0,h}^+ = N_{0,h}^- = N_{0,h} \tag{2}$$

where $\mu_j^{\pm}$ is the electrical mobility of positive and negative charge carriers in medium j, and $Z_j^{\pm}$ is charge number of positive and negative charge carriers in medium j.

The current density of each charge carrier type in the host and inclusion phases is the sum of current density due to drift current and diffusion current. In the absence of generation/recombination reactions, the transport equation representing conservation laws for charge-carrying species can be written as

$$\boldsymbol{j}_j^{\pm} = \boldsymbol{j}_{j,drift}^{\pm} + \boldsymbol{j}_{j,diffusion}^{\pm} = qN_j^{\pm}\mu_j\boldsymbol{e}_j \mp qD_j^{\pm}\nabla N_j^{\pm} \tag{3}$$

where $\boldsymbol{j}_j^{\pm}$ is the current density of positive and negative charge carriers, respectively, in medium j, $\mathbf{e}_j$ is the net electric field vector in medium j, and $D_j^{\pm}$ is the diffusion coefficient of positive and negative charge carriers, respectively, in medium j. When using the simplifying assumption for electrical mobility of charge carriers, as mentioned in equation 2, and Einstein's relationship of diffusion coefficient with electrical mobility, namely $D_j = \left(\mu_j k_B T\right)/q$, we obtain

$$D_h^+ = D_h^- = D_h;\ D_i^+ = D_i^- = D_i \tag{4}$$

By substituting $\boldsymbol{e}_j = -\nabla\varphi_j$ into the low-frequency limit of Maxwell's equations (induction neglected) and substituting equation 4 into equation 3, we express the charge species conservation condition as

$$\boldsymbol{j}_j^{\pm} = -qN_j^{\pm}\mu_j\nabla\varphi_j \mp qD_j\nabla N_j^{\pm} \tag{5}$$

where φ_j is the electrical potential in medium j. Equation 5 is Nernst-Planck's equation that describes the relationship of the flux of charge-carrying species to its concentration gradient and that to the applied electrical potential gradient in a given medium. Nernst-Planck's equation can alternatively be expressed as

$$\boldsymbol{j}_j^{\pm} = -D_j^{\pm}N_j^{\pm}\nabla\varphi_{cj}^{\pm} \tag{6}$$

where $\varphi_{cj}^{\pm} = k_B T\, ln\, N_j^{\pm} \pm qZ_j^{\pm}\varphi_j$ is the electrochemical potential of charge carriers. The continuity equation for charge carrier density based on mass conservation for each charge carrier type in an incompressible medium without any convective flow can be written as

$$\mp q\frac{\partial N_j^{\pm}}{\partial t} = \nabla\cdot\boldsymbol{j}_j^{\pm} \tag{7}$$

By applying equation 5 to equation 7, we obtain

$$\frac{\partial N_j^{+}}{\partial t} = \nabla\cdot\left(D_j\nabla N_j^{+} + \mu_j N_j^{+}\nabla\varphi_j\right) \tag{8}$$

and

$$\frac{\partial N_j^-}{\partial t} = \nabla \cdot \left(D_j \nabla N_j^- - \mu_j N_j^- \nabla \varphi_j\right) \tag{9}$$

The time derivative of equation 1 assuming axial symmetry is

$$\frac{\partial N_j^\pm}{\partial t} = i\omega c_j^\pm \tag{10}$$

where $c_j^\pm = c_j^\pm(r,t,\theta) = c_j^\pm(r)e^{i\omega t}\cos\theta$. We apply equation 10 to equations 8 and 9, then we add and subtract equation 8 and equation 9 to obtain equations 11 and 12 expressed as:

$$-iq\omega d_j = -2qN_{0,j}\mu_j \Delta\varphi_j - qD_j \Delta d_j \tag{11}$$

and

$$-iq\omega s_j = -qD_j \Delta s_j \tag{12}$$

where $d_j = c_j^+ - c_j^-$ represents net charge density variation, $s_j = c_j^+ + c_j^-$ represents total ion density variation, and Δ (∇^2) is Laplace's operator. Note d_j and s_j are finite everywhere in the representative volume, and for nonconductive particles, $d_i = s_i = 0$. We obtained equations 11 and 12 by assuming $d_j\mu_j \ll 1$ and $s_j\mu_j \ll 1$ as $\left|c_j^\pm\right| \leq N_{0,j}^\pm$.

Under the influence of an externally applied EM field, the distribution of charge carriers in both media leads to a time-varying electric potential that is expressed as $\varphi_j(r,t,\theta) = \varphi_j(r)e^{i\omega t}\cos\theta$. Using Gauss's law and equation 1, we obtain

$$\nabla \cdot \left(\varepsilon_j \boldsymbol{e}_j\right) = P_{f,j} = q\left(N_j^+ - N_j^-\right) = q\left(c_j^+ - c_j^-\right) = qd_j \tag{13}$$

where $P_{f,j}$ is the net free charge density in medium j due to charge redistribution in the presence of an externally applied EM field, $\boldsymbol{e}_j$, and $\varepsilon_j = \varepsilon_{r,j}\varepsilon_0$ is the dielectric permittivity of medium j, $\varepsilon_{r,j}$ is the relative permittivity of medium j, and $\varepsilon_0 = 8.854 \times 10^{-12}$ F/m is the vacuum permittivity. Equation 13 relates the spatial distribution of electric charge to the time-varying electric field. Assuming both media are linear, isotropic, and homogeneous, and that the electric field can be defined by a scalar electrical potential field, φ_j, we obtain

$$\nabla \cdot \left(\varepsilon_j \boldsymbol{e}_j\right) = -\nabla \cdot \left(\varepsilon_j \nabla \varphi_j\right) = -\varepsilon_j \Delta\varphi_j \tag{14}$$

By combining equations 13 and 14, we obtain an alternate expression of Poisson's equation, expressed as

$$\Delta\varphi_j = -\frac{qd_j}{\varepsilon_j} \tag{15}$$

Poisson's equation is applied to describe the electric field in terms of the electrical potential, the gradient of which governs electromigration in both media. By substituting equation 15 into equation 11, we obtain the Poisson-Nernst-Planck (PNP) equation, given by

$$-iq\omega d_j = 2q^2 N_{0,j}\mu_j d_j / \varepsilon_j - qD_j \Delta d_j \tag{16}$$

which can be re-written as

$$\Delta d_j = \left(\frac{i\omega}{D_j} + \frac{\sigma_j}{\varepsilon_j D_j}\right) d_j \tag{17}$$

where $\sigma_j = 2N_{0,j}\mu_j q$ is the electrical conductivity of medium j. We rewrite equations 17 and 12 as

$$\Delta d_j = {\gamma_j}^2 d_j \tag{18}$$

where

$${\gamma_j}^2 = \left(\frac{i\omega}{D_j} + \frac{\sigma_j}{\varepsilon_j D_j}\right) \tag{19}$$

and

$$\Delta s_j = {\xi_j}^2 s_j \tag{20}$$

where

$${\xi_j}^2 = \frac{i\omega}{D_j} \tag{21}$$

respectively. Equations 18 and 20 are Helmholtz partial differential equations (PDE) which can be solved to obtain distinct analytical expressions of d_j and s_j for the host and inclusion phases, respectively. Equation 18 is inserted into equation 15 to obtain the following Laplace PDE that can be solved for the electric potential field in the representative volume:

$$\Delta \vartheta_j = 0 \tag{22}$$

where

$$\vartheta_j = \varphi_j + \left(q d_j\right) / \left(\gamma_j^2 \varepsilon_j\right) \tag{23}$$

3.1.2.2. Solution of Helmholtz PDE

As mentioned before, for nonconductive inclusions, $d_i = s_i = 0$. So, we're solving the Helmholtz PDEs to obtain the distinct analytical expressions of d_h and s_h for the host phase. A sphere of radius equal to a exhibits dipolarizability (dipole moment) in the radial direction. Such an inclusion identifies a grain or vug. In order to compute the dipolarizability of the representative volume comprising a spherical inclusion in an electrolytic host, equation 18 can be expressed in spherical coordinates, assuming azimuthal symmetry, axial symmetry, and a separable solution (Young, 2009) for $d_h(r,\theta) = R_h(r)T_h(\theta)$, as

$$\frac{1}{R_h}\frac{\partial}{\partial r}\left(r^2\frac{\partial R_h}{\partial r}\right) - \gamma_h^2 r^2 + \frac{1}{T_h \sin\theta}\frac{\partial}{\partial\theta}\left(\frac{\sin\theta\, \partial T_h}{\partial\theta}\right) = 0 \tag{24}$$

and

$$\frac{1}{\sin\theta}\frac{\partial}{\partial\theta}\left(\frac{\sin\theta\, \partial T_h}{\partial\theta}\right) = -n(n+1)T_h \tag{25}$$

where *n* is an integer referring to the order of the standing wave solution. A standing wave solution (Young, 2009) to the above differential equation is

$$T_h = \sum_{n=1}^{\infty}\left[A_{n,h}P_n^0(\cos\theta) + B_{n,h}Q_n^0(\cos\theta)\right] \tag{26}$$

where P_n^0 and Q_n^0 are associated Legendre functions of the first and second kind (Weisstein, 2018a) respectively, of *n*-th order and $A_{n,h}$ and $B_{n,h}$ are unknown complex-valued coefficients of the general solution of the partial differential equation 25. Substituting equation 25 in equation 24, we obtain

$$\frac{\partial}{\partial r}\left(r^2\frac{\partial R_h}{\partial r}\right) - [\gamma_h^2 r^2 + n(n+1)]R_h = 0 \tag{27}$$

A standing wave solution to the above differential equation is

$$R_h = \sum_{n=1}^{\infty}\left[C_{n,h}i_n(r\gamma_h) + D_{n,h}k_n(r\gamma_h)\right] \tag{28}$$

where *n* is an integer for the standing wave solution (Young, 2009), i_n and k_n are the modified spherical Bessel function of the first and second kind (Weisstein, 2018b), respectively, of *n*-th order. $C_{n,h}$ and $D_{n,h}$ are unknown complex-valued coefficients of the general solution of the partial differential equation 27. i_n and k_n can be expressed in terms of modified Bessel function of the first and second kind, respectively, as $i_n(r\gamma_h) = \sqrt{\frac{\pi}{2r\gamma_h}}I_{n+\frac{1}{2}}(r\gamma_h)$ and $k_n(r\gamma_h) = \sqrt{\frac{2}{\pi r\gamma_h}}K_{n+\frac{1}{2}}(r\gamma_h)$, where $I_{n+\frac{1}{2}}$ and $K_{n+\frac{1}{2}}$ are the modified Bessel function of the first and second kind, respectively, of *(n+1/2)*-th order. To simplify the analytical derivation of our model, we reduce the series to a single term and use *n*=1 and $B_{n,h} = 0$ by considering the following symmetries of the charge density: (1) axial symmetry, (2) anti-symmetry with respect to $\theta,$ and (3) dipolar nature of the externally applied field. This reduces equations 28 and 26 to

$$R_h = C_h i_1(r\gamma_h) + D_h k_1(r\gamma_h) \tag{29}$$

and

$$T_h = A_h \cos\theta \tag{30}$$

respectively, where C_h, D_h, and A_h and are unknown complex-valued coefficients of the particular solution obtained from equations 26 and 28. The general representation of $d_h(r,\theta)$ can now be written, by combining equations 29 and 30, as

$$d_h(r,\theta) = A_h[C_h i_1(r\gamma_h) + D_h k_1(r\gamma_h)] \cos\theta \tag{31}$$

Using the condition that $d_h(r,\theta)$ should be finite at $r \to \infty$, we obtain a particular solution of d_h for the host phase that can be represented as

$$d_h(r,\theta) = B_{h1} k_1(r\gamma_h) \cos\theta \tag{32a}$$

or

$$d_h(r,\theta) = B_{h1}\left[e^{-r\gamma_h}\left(\frac{1}{r\gamma_h} + \frac{1}{(r\gamma_h)^2}\right)\right] \cos\theta \tag{32b}$$

where B_{h1} is unknown complex-valued coefficient of the particular solution in the host medium obtained from equation 31. Note when $r \to \infty$, $d_h(r,\theta) = 0$. Repeat the above procedure, we can obtain a particular solution of s_h for the host phase from equation 20 that can be represented as

$$s_h(r,\theta) = B_{h2} k_1(r\xi_h) \cos\theta \tag{33a}$$

or

$$s_h(r,\theta) = B_{h2}\left[e^{-r\xi_h}\left(\frac{1}{r\xi_h} + \frac{1}{(r\xi_h)^2}\right)\right] \cos\theta \tag{33b}$$

where B_{h2} is unknown complex-valued coefficient of the particular solution in the host medium.

3.1.2.3. Solution of Laplace PDE

The Laplacian partial differential equation (PDE) must be solved to obtain the electric potential field in the representative volume. Assuming azimuthal symmetry and a separable solution for $\vartheta_j(r,\theta,\varphi) = R_{\epsilon j}(r)T_{\epsilon j}(\theta)$, equation 22 can be expressed in spherical coordinates as

$$\Delta\vartheta_j = \frac{1}{R_{\epsilon j}}\frac{\partial}{\partial r}\left(r^2\frac{\partial R_{\epsilon j}}{\partial r}\right) + \frac{1}{T_{\epsilon j}\sin\theta}\frac{\partial}{\partial\theta}\left(\frac{\sin\theta\,\partial T_{\epsilon j}}{\partial\theta}\right) = 0 \tag{34}$$

Assuming axial symmetry, a general solution (Hogg, 2001) to the above PDE can be expressed as

$$\vartheta_j(r,\theta) = \sum_{n=0}^{\infty}\left[A_{n,j}r^n + C_{n,j}r^{-(n+1)}\right]\left[E_{n,j}P_n^0(cos(n\theta)) + F_{n,j}Q_n^0(sin(n\theta))\right] \tag{35}$$

where *n* is an integer and $A_{n,j}$, $C_{n,j}$, $E_{n,j}$, and $F_{n,j}$ are unknown complex-valued coefficients of the general solution of the PDE expressed in equation 34. For analytical modeling purposes for our model, we assume *n*=1 and $F_{n,j} = 0$, $A_{0,j} = 0$ and $C_{0,j} = 0$, which ensures remaining terms satisfy the polar angle dependence of the model. Simplified representation of equation 35 is expressed as

$$\vartheta_j(r,\theta) = \left(A_{1,j}r + C_{1,j}r^{-2}\right)E_{1,j}\, cos\,\theta \tag{36a}$$

which can be rewritten using equation 23 as

$$\varphi_j(r,\theta) = \left(A_j r + C_j r^{-2}\right) cos\,\theta - \frac{q d_j(r,\theta)}{\gamma_j^2 \varepsilon_j} \tag{36b}$$

Using the condition that $d_i = 0$ and φ_i should be finite when $r \to 0$, we can obtain $C_i = 0$. So, a standing wave representation of equation 36b for the nonconductive inclusion phase is

$$\varphi_i(r,\theta) = A_i r\, cos\,\theta \tag{37}$$

where A_i is unknown complex-valued coefficient of the particular solution in the nonconductive inclusion phase obtained from equation 36b. Using the condition when $r \to \infty$, $d_h = 0$, we can obtain $A_h = -E_0$. A standing wave representation of equation 36b for the host phase, using equation 32b, is

$$\varphi_h(r,\theta) = (-E_0 r + C_h r^{-2})\, cos\,\theta - \frac{qB_{h1}}{\gamma_h^2\varepsilon_h}\left[e^{-r\gamma_h}\left(\frac{1}{r\gamma_h} + \frac{1}{(r\gamma_h)^2}\right)\right] cos\,\theta \tag{38}$$

where C_h is unknown complex-valued coefficient of the particular solution in the host obtained from equation 36b and E_0 is the amplitude of the externally applied electric field.

3.1.2.4. Boundary conditions

To obtain an expression for the dipolarizability (dipole moment), we need first to identify the boundary conditions (Grosse, 1988):

a) Continuity of the electric potential at the interface.

$$\varphi_i(r = a) = \varphi_h(r = a) \tag{39a}$$

b) Discontinuity of the normal component of the displacement current at the interface because of the surface charge distribution on the inclusion phase. This boundary condition is derived from Gauss' Law.

$$\varepsilon_i \frac{\partial \varphi_i}{\partial r}\bigg|_{r=a} - \varepsilon_h \frac{\partial \varphi_h}{\partial r}\bigg|_{r=a} = \rho \cos\theta \tag{39b}$$

c) Continuity of the surface charge density at the host-inclusion interface qualitatively expressed as: Rate of change of surface charge density = normal drift/conduction current at the interface due to potential gradient arising from the external electromagnetic field + normal diffusion current due to concentration gradient in the host media at the interface + tangential conduction current due to the potential gradient arising from the surface-charge-bearing inclusion phase. In other words, this boundary condition shows that the time derivative of surface charge density in the counterion layer is equal to the sum of the normal conduction and diffusion current due to potential and concentration difference, separately, from the host medium and the tangential conduction current due to potential from the inclusion phase.

$$-i\omega\rho \cos\theta = -\frac{\sigma_h}{2}\frac{\partial \varphi_h}{\partial r}\bigg|_{r=a} - qD_h \frac{\partial c_h^+}{\partial r}\bigg|_{r=a} + \frac{2\lambda}{a} A_i \cos\theta \tag{39c}$$

d) The normal component of the current density of negative ions in the host medium must vanish at the interface due to the assumption that the negative ions are excluded from the counterion layer.

$$\boldsymbol{j}_h^- = -\frac{\sigma_h}{2}\frac{\partial \varphi_h}{\partial r}\bigg|_{r=a} + qD_h \frac{\partial c_h^-}{\partial r}\bigg|_{r=a} = 0 \tag{39d}$$

e) Due to the application of the external electric field, we use a simplifying assumption that the relative change of the positive ion density in the counterion layer (which is assumed to be negligibly thin) and that in the host medium must be equal because the positive ions in the host medium can freely exchange with the ions in the counterion layer.

$$\frac{c_h^+(r = a, \theta)}{N_{0,h}} = \frac{\rho \cos\theta}{\rho_0} \tag{39e}$$

where ρ_0 is the initial equilibrium surface change density in the counterion layer and ρ is the net resultant surface charge density in the counterion layer after the application of electric field.

3.1.2.5. Solution for the dipolarizability

Using boundary condition (39a), equations 37 and 38 can be equated on the surface of the sphere of radius equal to a. The resulting equation can be abbreviated as

$$-E_0 a + \frac{C_h}{a^2} - E_h B_{h1} = A_i a \tag{40a}$$

where

$$E_h = \frac{q}{\gamma_h^2 \varepsilon_h} e^{-a\gamma_h} \left[\frac{1}{a\gamma_h} + \frac{1}{(a\gamma_h)^2}\right] \tag{40b}$$

The equation obtained using boundary condition (39b) at the surface of the sphere can be abbreviated as

$$\varepsilon_h \left(E_0 + \frac{2C_h}{a^3} - G_h B_{h1}\right) + \varepsilon_i A_i = \rho \tag{41a}$$

where

$$G_h = \frac{q}{\gamma_h \varepsilon_h} e^{-a\gamma_h} \left[\frac{1}{a\gamma_h} + \frac{2}{(a\gamma_h)^2} + \frac{2}{(a\gamma_h)^3}\right] \tag{41b}$$

Boundary condition (39c) gives us the following abbreviated equation:

$$i\omega\rho = -\frac{\sigma_h}{2} E_0 - \frac{\sigma_h C_h}{a^3} + \frac{\sigma_h}{2} G_h B_{h1} - \frac{D_h}{2} \gamma_h^2 G_h B_{h1} \varepsilon_h - \frac{D_h}{2} \xi_h^2 L_h B_{h2} \varepsilon_h - \frac{2\lambda}{a} A_i \tag{42a}$$

where

$$L_h = \frac{q}{\xi_h \varepsilon_h} e^{-a\xi_h} \left[\frac{1}{a\xi_h} + \frac{2}{(a\xi_h)^2} + \frac{2}{(a\xi_h)^3}\right] \tag{42b}$$

Similarly, the equation obtained using boundary condition (39d) can be abbreviated as

$$\frac{\sigma_h}{2} E_0 + \frac{\sigma_h C_h}{a^3} - \frac{\sigma_h}{2} G_h B_{h1} = \frac{D_h}{2} \xi_h^2 L_h B_{h2} \varepsilon_h - \frac{D_h}{2} \gamma_h^2 G_h B_{h1} \varepsilon_h \tag{43}$$

For boundary condition (39e), we assume the electrical mobilities in the two regions are the same to re-write this boundary condition as

$$2qc_h^+(r = a) = \frac{\rho \sigma_h}{\lambda} \tag{44}$$

After solving equations 40a, 41a, 42a, 43 and 44, we obtain the dipolarizability (dipolar field coefficient) of the representative volume comprising a spherical nonconductive inclusion in an electrolytic host as

$$f_{ncond}(\omega) = \frac{C_h}{E_0 a^3} = \frac{Q(R + A) - P}{Q(R - 2A) + 2P} \tag{45}$$

where

$$A = \frac{1}{a^2} \tag{45a}$$

$$P = \gamma_h^2 + \xi_h^2 \frac{G}{H} + \frac{2G}{a^2 L} \tag{45b}$$

$$Q = \frac{1}{iF + 1}\left[2 - \frac{a^2 \xi_h^2}{H}\left(\frac{L}{iF} + E\right) - \frac{2E}{L}\right] \tag{45c}$$

$$R = \frac{P}{Q}\left(\frac{iFE + L}{iF + 1}\right) \tag{45d}$$

$$H = \frac{aL_h}{F_h}, G = \frac{aG_h}{E_h}, L = \frac{2\lambda}{a\sigma_h}, E = \frac{\varepsilon_i}{\varepsilon_h}, F = \frac{\omega\varepsilon_h}{\sigma_h} \tag{45e}$$

$$F_h = \frac{q}{\xi_h^2 \varepsilon_h} e^{-a\xi_h}\left[\frac{1}{a\xi_h} + \frac{1}{(a\xi_h)^2}\right] \tag{45f}$$

3.1.3. PPIP model

The PPIP model was first developed and published by Misra et al. (2016b). The derivation procedure is similar to that of the SCAIP model. The final expression of PPIP model was obtained by applying different boundary conditions.

In this thesis, perfectly polarized interfacial polarization (PPIP) model is applied to investigate interfacial polarization phenomena around conductive particle. Figure 3.2 shows PPIP phenomena in a representative volume of a dilute mixture of uniformly distributed electrically conductive spherical inclusions in an electrolyte-saturated host medium, where interfacial polarization is independent of the direction of the externally applied electric field due to spherical symmetry.

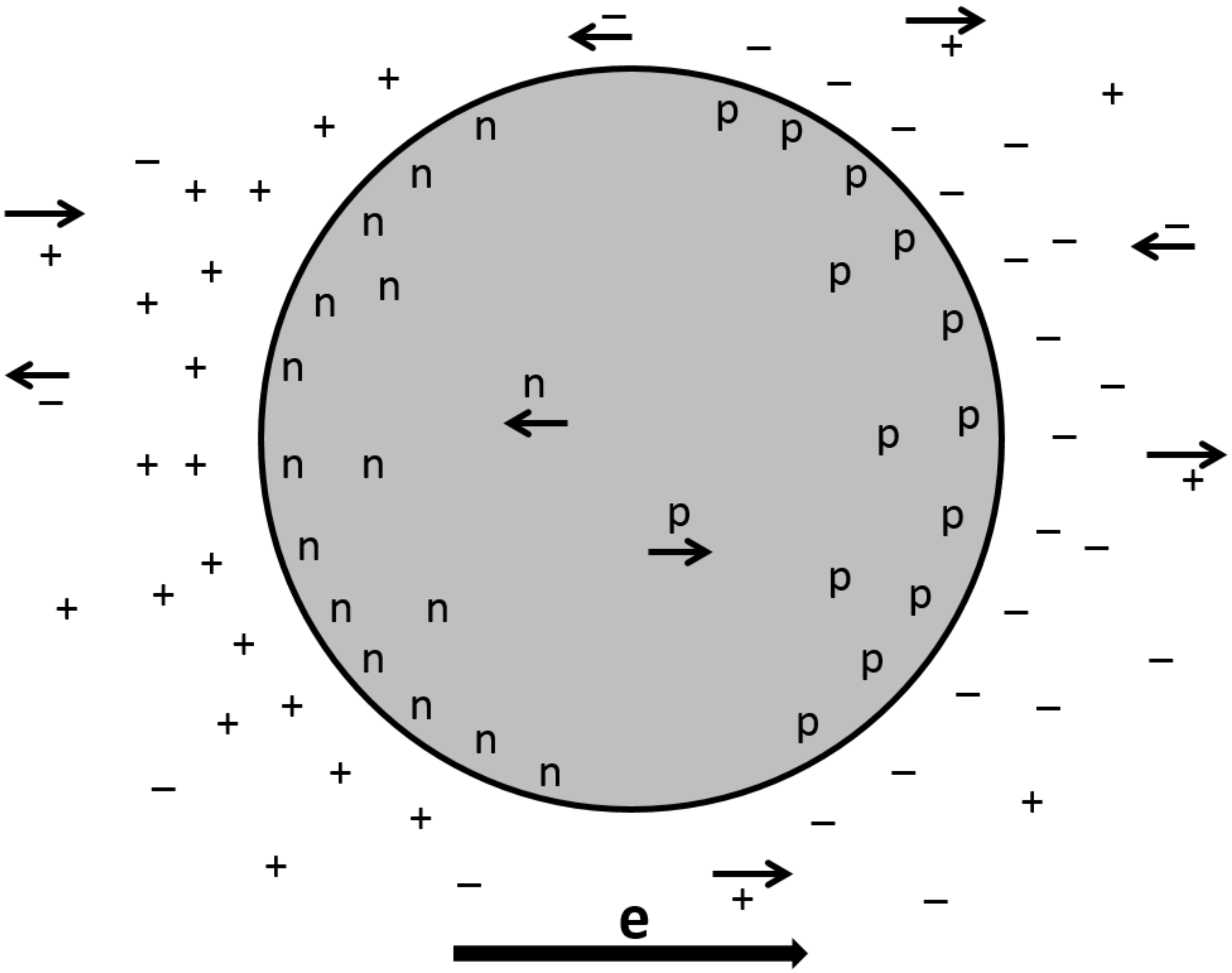

Figure 3.2. Cross-section of a perfectly polarized conductive spherical inclusion surrounded by an ionic host medium. Charge carriers in the ionic host medium are cations, identified by "+" symbol, and anions, identified by "-" symbol. Charge carriers in the conductive spherical inclusion are n- and p-charge carriers, identified by symbol "n" and "p", respectively. The direction of the externally applied electrical field, e, is identified with a bold arrow next to the symbol "e". The direction of movement of the four different types of charge carriers is represented by the arrow next to the symbols of the charge carriers.

The phenomenological basis of interfacial polarization considered in this work builds on the mechanistic descriptions outlined by Revil et al. (2015). Charge carriers in conductive minerals have higher mobility compared to ions in porous geomaterials. In the presence of an externally applied EM field, charge carriers in the disseminated electrically conductive inclusions migrate faster and accumulate at impermeable interfaces. Consequently, electrically conductive inclusions behave as dipoles in the presence of an externally applied electric field. Subsequently, charge carriers in the host medium migrate and accumulate on host-inclusion interfaces under the influence of the externally applied electric field and that of the induced charges in conductive inclusions.

In the absence of an externally applied electric field, a negligible initial surface charge is assumed on electrically conductive inclusions. Thus, there is typically a negligible double layer around the surface of electrically conductive inclusions, whereby the surface conductance of a conductive inclusion is negligible. Similar assumptions are made in electrochemistry and colloid science with respect to electrochemical relaxation around metallic surfaces (Chu and Bazant, 2006). Also, we assume absence of redox-active species and neglect the influence of pH of pore water (Revil et al., 2015). The host and inclusion phases can be modeled as an electrically conductive, insulating, or dielectric material. Also, pore-filling fluid can be modeled as electrically conductive (e.g. brine) or non-conductive material (e.g. oil).

3.1.3.1. PPIP model development

The development of the PPIP model (Misra et al., 2016b) is very similar to that of the SCAIP model. For PPIP model development, spontaneous initial accumulation of charges is assumed to be absent on the host-inclusion interfaces. At time $t < 0$, electro-neutrality is assumed throughout the system.

3.1.3.2. Solution of Helmholtz PDE

The above-mentioned equation 18 must be solved to obtain an analytical expression for d_j in the host and inclusion phases around the perfectly polarized host-inclusion interface of conductive spherical inclusion. Recall that $d_j = c_j^+ - c_j^-$ represents net charge density variation, where $c_j^{\pm}$ is the charge density variation near the host-inclusion interface in medium j due to the externally applied electric field. Expression for $d_h(r,\theta)$ for the mixture containing conductive spherical inclusion is the same as that for the mixture containing nonconductive spherical inclusion. Using the condition that $d_i(r,\theta)$ should be finite at $r \rightarrow 0$, we obtain a particular solution for d_i for the mixture containing conductive spherical inclusion that can be represented as

$$d_i(r,\theta) = B_i i_1(r\gamma_i) \cos\theta \qquad (46a)$$

or

$$d_i(r,\theta) = B_i\left[\frac{cosh(r\gamma_i)}{r\gamma_i} - \frac{sinh(r\gamma_i)}{(r\gamma_i)^2}\right]cos\,\theta \qquad (46b)$$

where B_i is unknown complex-valued coefficient of the particular solution in the inclusion phase obtained from equation 31, substituting the subscript h with i. Note when $r \rightarrow 0$, it is assumed that $d_i(r,\theta) = 0$.

3.1.3.3. Solution of Laplace PDE

The above-mentioned equation 22 must be solved to obtain the electric potential field in the representative volume. The expression for $\varphi_h(r,\theta)$ for the mixture containing conductive spherical inclusion is the same as that for the mixture containing nonconductive spherical inclusion. Using the condition when $r \rightarrow 0$, $d_i = 0$ and φ_i should be finite, we can obtain $C_i = 0$. A standing wave representation of equation 36b for the conductive inclusion phase, using equation 46b, is

$$\varphi_i(r,\theta) = A_i r\,cos\,\theta - \frac{qB_i}{\gamma_i^2\varepsilon_i}\left[\frac{cosh(r\gamma_i)}{r\gamma_i} - \frac{sinh(r\gamma_i)}{(r\gamma_i)^2}\right]cos\,\theta \qquad (47)$$

where A_i is unknown complex-valued coefficient of the particular solution in the conductive inclusion phase obtained from equation 36b.

3.1.3.4. Boundary conditions

To obtain an expression for the dipolarizability, we need first to identify the boundary conditions (Grosse and Foster, 1987):

a) Assuming a zero-intrinsic capacitance of the host-inclusion interface, the electric potential must be continuous at the interface.

$$\varphi_i(r=a) = \varphi_h(r=a) \qquad (48a)$$

b) The normal component of the displacement current must be continuous at the interface. This condition corresponds to the fact that there is no net surface-charge distribution on an electrically conductive inclusion phase.

$$\varepsilon_i \left.\frac{\partial\varphi_i}{\partial r}\right|_{r=a} = \varepsilon_h \left.\frac{\partial\varphi_h}{\partial r}\right|_{r=a} \qquad (48b)$$

c) The normal component of the current density must vanish at the interface for both media. This condition expresses the fact that in the absence of transport of charge carriers and exchange of charges along the interface, the diffusive and electro-migrative currents must cancel each other at the interface. Our focus is perfectly polarizable or completely blocking interfaces without Faradic processes, wherein fluxes of charge carriers must vanish on both sides of the interface. Note that this boundary condition is used to obtain two equations: one for the outer volume of the sphere in the host medium, and the other for the inner volume of the sphere in the inclusion medium.

$$\boldsymbol{j}_j^+ + \boldsymbol{j}_j^- = -2N_{0,j}q\mu_j \frac{\partial \varphi_j}{\partial r}\bigg|_{r=a} - qD_j \frac{\partial d_j}{\partial r}\bigg|_{r=a} = 0 \; (j = h \; or \; i) \tag{48c}$$

3.1.3.5. Solution for the dipolarizability

Using boundary condition (48a), equations 47 and 38 can be equated on the surface of the sphere of radius equal to a. The resulting equation can be abbreviated as

$$-E_0 a + \frac{C_h}{a^2} - E_h B_h = A_i a - F_i B_i \tag{49a}$$

where

$$F_i = \frac{q}{\gamma_i^2 \varepsilon_i}\left[\frac{cosh(a\gamma_i)}{a\gamma_i} - \frac{sinh(a\gamma_i)}{(a\gamma_i)^2}\right] \tag{49b}$$

The equation obtained using boundary condition (48b) at the surface of the sphere can be abbreviated as

$$\varepsilon_h\left(-E_0 - \frac{2C_h}{a^3} + G_h B_h\right) = \varepsilon_i(A_i + H_i B_i) \tag{50a}$$

where

$$H_i = \frac{q}{\gamma_i \varepsilon_i}\left[\frac{2\,cosh(a\gamma_i)}{(a\gamma_i)^2} - \frac{sinh(a\gamma_i)}{a\gamma_i} - \frac{2sinh(a\gamma_i)}{(a\gamma_i)^3}\right] \tag{50b}$$

Similarly, the equation obtained using boundary condition (48c) at the outer surface of the sphere in the host medium can be abbreviated as

$$C_h = -a^3\left(\frac{E_0}{2} + \frac{i\omega\varepsilon_h G_h B_h}{2\sigma_h}\right) \tag{51}$$

On the other hand, the equation obtained using boundary condition (48c) at the inner surface of the sphere in the inclusion medium can be abbreviated as

$$A_i = \frac{i\omega\varepsilon_i H_i B_i}{\sigma_i} \tag{52}$$

Solve equations 49a, 50a, 51, and 52, we obtain the dipolarizability (dipolar field coefficient) of the representative volume comprising a spherical conductive inclusion in an electrolytic host as

$$f_{cond}(\omega) = \frac{C_h}{E_0 a^3} = -\frac{1}{2} + \frac{3}{2} \frac{i\omega}{\left[\frac{2}{a}\frac{\sigma_h}{\varepsilon_h}\frac{E_h}{G_h} - \frac{2}{a}\frac{\sigma_h^*}{\sigma_i^*}\frac{\sigma_i}{\varepsilon_i}\frac{F_i}{H_i} + i\omega\left(\frac{2\sigma_h^*}{\sigma_i^*} + 1\right)\right]} \tag{53}$$

where $\sigma_h^* = \sigma_h + i\omega\varepsilon_h$ is the complex conductivity of the host medium and $\sigma_i^* = \sigma_i + i\omega\varepsilon_i$ is the complex conductivity of the inclusion phase.

3.1.4. Effective medium theory and the expression of PS model

We aim to develop a mechanistic model to quantify the conductivity and permittivity (complex conductivity) of geological mixtures containing clay particles, conductive minerals, oil and water. This new model is referred herein as the PPIP-SCAIP (PS) model. To that end, PS model accounts for the interfacial polarization (IFP) due to surface conductance of clays and sands and the IFP due to conductive mineral grains at various water saturations. PS model development requires two steps: first, using PPIP model and SCAIP model to quantify the IFP of the representative volume (as described previously), followed by using effective medium theory to accurately combine the IFP of various representative volumes present in the mixture.

We apply the effective-medium theory to determine the effective complex electrical conductivity (σ_{eff}^*) of the mixture (Grosse and Barchini, 1992) after we obtain the expressions of dipolarizability for spherical nonconductive and conductive particles surrounded by the electrolyte-saturated host medium. For the development of our model, as stated in the previous sections, PNP equations are first used to obtain dipolarizabilities (dipole moment), which are microscopic electrical properties, for the representative volume containing either spherical nonconductive or conductive particle. In the derivations of dipolarizabilities, we neglect multipoles effect because their magnitude decreases with inverse power of distance (Sihvola, 2007). Monopole effects are also neglected since there is zero net charge due to the assumed electroneutrality. The macroscopic electrical properties are then computed using effective-medium formulations based on the theory that a material composed of a mixture of distinct homogeneous media can be seen as a homogeneous material at a sufficiently large observation scale (Giordano, 2003).

In this thesis, we obtain the effective electrical properties using a Maxwell Garnett type effective-medium formulation. To meet the requirements of the formulation, the volume fraction of nonconductive and conductive inclusions in the mixture should be less than 20% (Revil et al., 2015). Subsurface water-bearing reservoir rocks have less than 10% volume fraction of conductive mineral inclusions but the volume fraction of non-conductive particles possessing surface charge (e.g. clay and sand) can exceed 20%. Moreover, we invoke the PNP equations in the bulk electrolyte that introduces a decaying length scale, where the Maxwell Garnett formula may become invalid at even lower concentration of inclusion phase (Hou et al., 2018). It is also important to mention this formulation used in the calculation neglects the EM interaction between the inclusions and other components. Due to the assumed dilution of the uniformly distributed inclusion phase, individual elements of the dispersed phase are assumed to be isolated and not in contact with each other. Like other mixing theories, our model includes the assumption that the magnitude of spatial variations of the electric field is smaller than the magnitude of variations in the intrinsic electrical properties and geometrical structures. Moreover, all calculations are performed using a quasi-static assumption that requires the size of heterogeneities to be much smaller than the wavelength of the applied EM field (Cosenza et al., 2009). Also, when dealing with a lossy medium, the skin depth of the EM wave must be considered to avoid strong attenuation of the field amplitudes in the conductive heterogeneities. Most importantly, due to the implementation of the PNP equations, our effective-medium formulations unlike other theories (Giordano, 2003) explicitly accounts for the characteristic lengths of heterogeneities, resulting in a physically consistent way to account for the perturbation due to nonconductive or conductive inclusions.

The effective medium formulation used by Misra et al. (2016b) is modified to model the complex conductivity response of multiphase mixtures containing spherical nonconductive and conductive particles, which can be expressed as

$$\frac{\sigma_{\hat{n},eff}^{*} - \sigma_{h}^{*}}{\sigma_{\hat{n},eff}^{*} + 2\sigma_{h}^{*}} = \phi_{cond} f_{cond}(\omega) + \phi_{ncond} f_{ncond}(\omega) \tag{54}$$

where $\sigma^{*} = \sigma + i\omega\varepsilon$ is a representation of the complex conductivity of a material, $\sigma_{\hat{n},eff}^{*}$ is the effective complex conductivity of the geological mixture directed along the $\hat{n}$ unit vector that can be measured with an externally applied electric field directed along the $\hat{n}$ unit vector and σ_{h}^{*} is the complex-valued conductivity of the homogenous isotropic host material that surrounds the particles. ϕ_{cond} and ϕ_{ncond} is the volume fraction of the conductive and nonconductive inclusion phase in the mixture, respectively. $f_{cond}(\omega)$ and $f_{ncond}(\omega)$ is the dipolarizability of conductive and nonconductive inclusion phase, respectively, along the direction of $\hat{n}$ unit vector, along which the externally applied electric field is directed.

3.2. Wettability Model

The mechanistic model developed by us is the first of its kind model for subsurface characterization, engineering, and geosciences, with a special emphasis on upstream oil and gas exploration and production. For developing the new mechanistic model, we first solve Young-Laplace equation for a spherical grain in a mixture of oil and water, with known proportion of oil and water. Young-Laplace equation determines the shape of the oil-water interface (meniscus) at equilibrium by applying appropriate boundary conditions. In doing so, we obtain the expression of wetting angle of the conductive or surface-charge-bearing particle as a function of contact angle of the solid particle and the water-oil mixture. The aim of this mechanistic model is to quantify the wettability effects of solid particles on the electromagnetic properties of a mixture of solids and fluids for various fluid saturations and solid wettability.

3.2.1. Model description

At the representative volume level, we assume the oil layer stays at the top, water layer goes to the bottom, the two layers have one common interface, and they are spread across a length scale that is orders of magnitude larger than the size of the spherical solid particle. The height of these two layers are in proportion to the corresponding fluid saturations. The spherical solid particle suspends at the oil-water interface, as shown in the Figure 3.3. The wetting phase will try to surround the solid particle to satisfy the contact angle. The climb of oil-water interface generates a wetting angle, which represents the degree of exposure of the particle to the wetting phase. The interfacial polarization phenomena due to such solid particles are entirely governed by the extent to which the solid particle is surrounded by water versus oil, which is governed by the oil saturation and wettability of the solid particle.

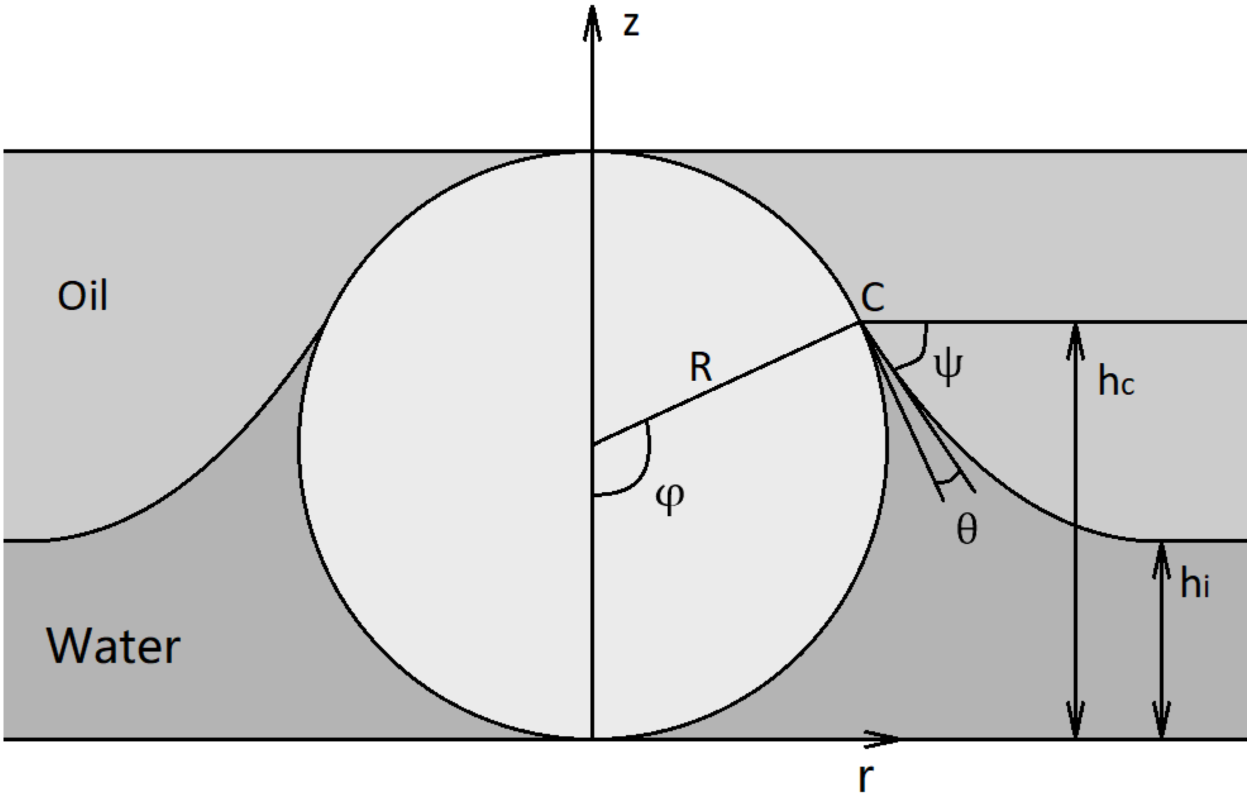

Figure 3.3. Cross-section of a spherical graphite particle suspended in an oil-water medium. In the picture, C denotes the point where the oil-water interface contacts the particle surface. θ is the contact angle. φ is the wetting angle. ψ is the angle between oil-water interface and the horizon (x-axis) at point C. R is the radius of graphite particle. h_i is the height of oil-water interface in the absence of wetting of graphite (far-field height). h_c is the height where the oil-water interface contacts the particle surface, $h_c = R(1 - cos\,\varphi)$. r is the distance from vertical axis z and $h(r)$ is the height of oil-water interface at any distance r away from the vertical axis z.

We assume the far-field height of oil-water interface in the absence of wetting, h_i, have linear relationship with oil saturation:

$$h_i = 2R(1 - S_o) \tag{1}$$

where S_o is oil saturation, such that $h_i = 0$ when the representative volume has 100% saturation of oil and $h_i = 2R$ when the representative volume has 100% saturation of water. S_o can be related to the volume fraction of oil in the mixture, ϕ_o, using the following equation:

$$S_o = \frac{\phi_o}{\phi} \tag{2}$$

where ϕ denotes porosity of the mixture containing sand, clay, graphite, water, and oil.

3.2.2. Young-Laplace equation

The shape of the oil-water interface (meniscus) at equilibrium is described by Young-Laplace equation (Cavallaro Jr, 2012):

$$\Delta p = 2H\sigma \tag{3}$$

where Δp, with a unit of Pa, is Laplace pressure defined as the pressure difference between the inside and the outside of the curved surface that forms the boundary between oil and water phase. H, with a unit of m^{-1}, is mean curvature of the meniscus surface and σ, with a unit of N/m, is interfacial tension between oil and water. Laplace pressure can be expressed by

$$\Delta p = (\rho_w - \rho_o)g[h(r) - h_i] \tag{4}$$

where ρ_w and ρ_o is density of water and oil, respectively, and g denotes gravitational acceleration. The mean curvature can be expressed as a surface divergence (Kralchevsky et al., 1994):

$$2H = \nabla \cdot \left[\frac{\nabla h}{\sqrt{1 + (\nabla h)^2}}\right] \tag{5}$$

Bond number is defined by $B_o = \frac{(\rho_w - \rho_o)gR^2}{\sigma}$, which is the ratio between gravity force and surface tension force. Assume typical values: $\rho_o = 800\,kg/m^3$, $\rho_w = 1000\,kg/m^3$, $g = 9.8\,N/kg$, $R = 200\mu m$, and $\sigma = 0.05\,N/m$, we can calculate $B_o = 0.0016 \ll 1$. Such a small Bond number represents negligible gravity force and the mean curvature remains constant everywhere on the interface, which renders a small slope assumption. Under this condition, we have $(\nabla h)^2 \ll 1$, the mean curvature simplifies to (Cavallaro Jr, 2012):

$$2H = \nabla \cdot \nabla h = \Delta h \tag{6}$$

Since the meniscus surface is axisymmetric, the mean curvature can be further simplified under cylindrical coordinates as

$$2H = \frac{1}{r}\frac{\partial}{\partial r}\left(r\frac{\partial h}{\partial r}\right) = h'' + \frac{h'}{r} \tag{7}$$

where h' and h'' represents $\frac{dh}{dr}$ and $\frac{d^2h}{dr^2}$, respectively. Substitute equation 4 and 7 into 3, the Young-Laplace equation becomes:

$$\frac{(\rho_w - \rho_o)g[h(r) - h_i]}{\sigma} = h'' + \frac{h'}{r} \tag{8}$$

We also define some dimensionless variables to normalize equation 8:

$$\hat{r} = \frac{r}{L_c}, \hat{h} = \frac{h}{L_c}, G(\hat{r}) = \frac{h(r) - h_i}{L_c} \tag{9}$$

where L_c is capillary length, defined by

$$L_c = \sqrt{\frac{\sigma}{(\rho_w - \rho_o)g}} \tag{10}$$

Substituting equation 9 and 10 into 8, we can obtain a modified Bessel differential equation (Fiegel et al., 2005):

$$G'' + \frac{G'}{\hat{r}} - G = 0 \tag{11}$$

where G' and G'' represents $\frac{dG}{d\hat{r}}$ and $\frac{d^2G}{d\hat{r}^2}$, respectively. The solution of the differential equation 11 consists of modified Bessel functions of the first and second kind of order 0, which is shown below:

$$G = c_1 I_0(\hat{r}) + c_2 K_0(\hat{r}) \tag{12}$$

To solve the equation 12, we need to identify two boundary conditions:

a) The height of oil-water interface at infinite distance, $h(r)|_{r\to\infty}$, is equal to h_i, which gives

$$\lim_{\hat{r}\to\infty} G = 0 \tag{13a}$$

b) The height of oil-water interface at distance $r = R\, sin\, \varphi$ is h_c, which gives

$$G\left(\hat{r} = \sqrt{B_o}\, sin\, \varphi\right) = \hat{h}_c - \hat{h}_i \tag{13b}$$

Using boundary condition 13a, we can obtain $c_1 = 0$. Using boundary condition 13b, we can obtain $c_2 = \frac{\hat{h}_c - \hat{h}_i}{K_0\left(\sqrt{B_o}\, sin\, \varphi\right)}$, where K_0 is modified Bessel function of the second kind of order 0. Substitute c_1, c_2 and equation 9 into equation 12, we can obtain the expression for the shape of the oil-water interface:

$$\hat{h} = \hat{h}_i + \frac{\hat{h}_c - \hat{h}_i}{K_0\left(\sqrt{B_o}\, sin\, \varphi\right)} K_0(\hat{r}) \tag{14}$$

3.2.3. Wetting angle determination

At point C, we have

$$tan\, \psi = -\left.\frac{dh}{dr}\right|_{r = R\, sin\, \varphi} = -\left.\frac{d\hat{h}}{d\hat{r}}\right|_{\hat{r} = \sqrt{B_o}\, sin\, \varphi} = \frac{\hat{h}_c - \hat{h}_i}{K_0\left(\sqrt{B_o}\, sin\, \varphi\right)} K_1\left(\sqrt{B_o}\, sin\, \varphi\right) \tag{15}$$

where K_1 is modified Bessel function of the second kind of order 1. The angle ψ can be calculated as

$$\psi = tan^{-1}(tan\,\psi) = tan^{-1}\left[\frac{\hat{h}_c - \hat{h}_i}{K_0\left(\sqrt{B_o}\,sin\,\varphi\right)}K_1\left(\sqrt{B_o}\,sin\,\varphi\right)\right] \tag{16}$$

The three angles, θ, φ and ψ, can be related using equation

$$180 = \theta + \varphi + \psi \tag{17}$$

Substitute equation 16 to 17, we have

$$\varphi = 180 - \theta - tan^{-1}\left[\frac{\hat{h}_c - \hat{h}_i}{K_0\left(\sqrt{B_o}\,sin\,\varphi\right)}K_1\left(\sqrt{B_o}\,sin\,\varphi\right)\right] \tag{18a}$$

It's hard to obtain an analytical solution for wetting angle φ from equation 18a because it is a transcendental equation. But we can find the numerical solution using computer. To solve this, we move the left item to the right in equation 18a to define a function:

$$f(\varphi) = 180 - \varphi - \theta - tan^{-1}\left[\frac{\hat{h}_c - \hat{h}_i}{K_0\left(\sqrt{B_o}\,sin\,\varphi\right)}K_1\left(\sqrt{B_o}\,sin\,\varphi\right)\right] \tag{18b}$$

and find the φ which makes $f(\varphi) = 0$ using Newton-Raphson method. To ensure that the equation has a unique solution, we examine the monotonicity of the function by plotting $f(\varphi)$, as shown in Figure 3.4. The plot shows that $f(\varphi)$ is a monotonic function in the range of $0° < \varphi < 180°$.

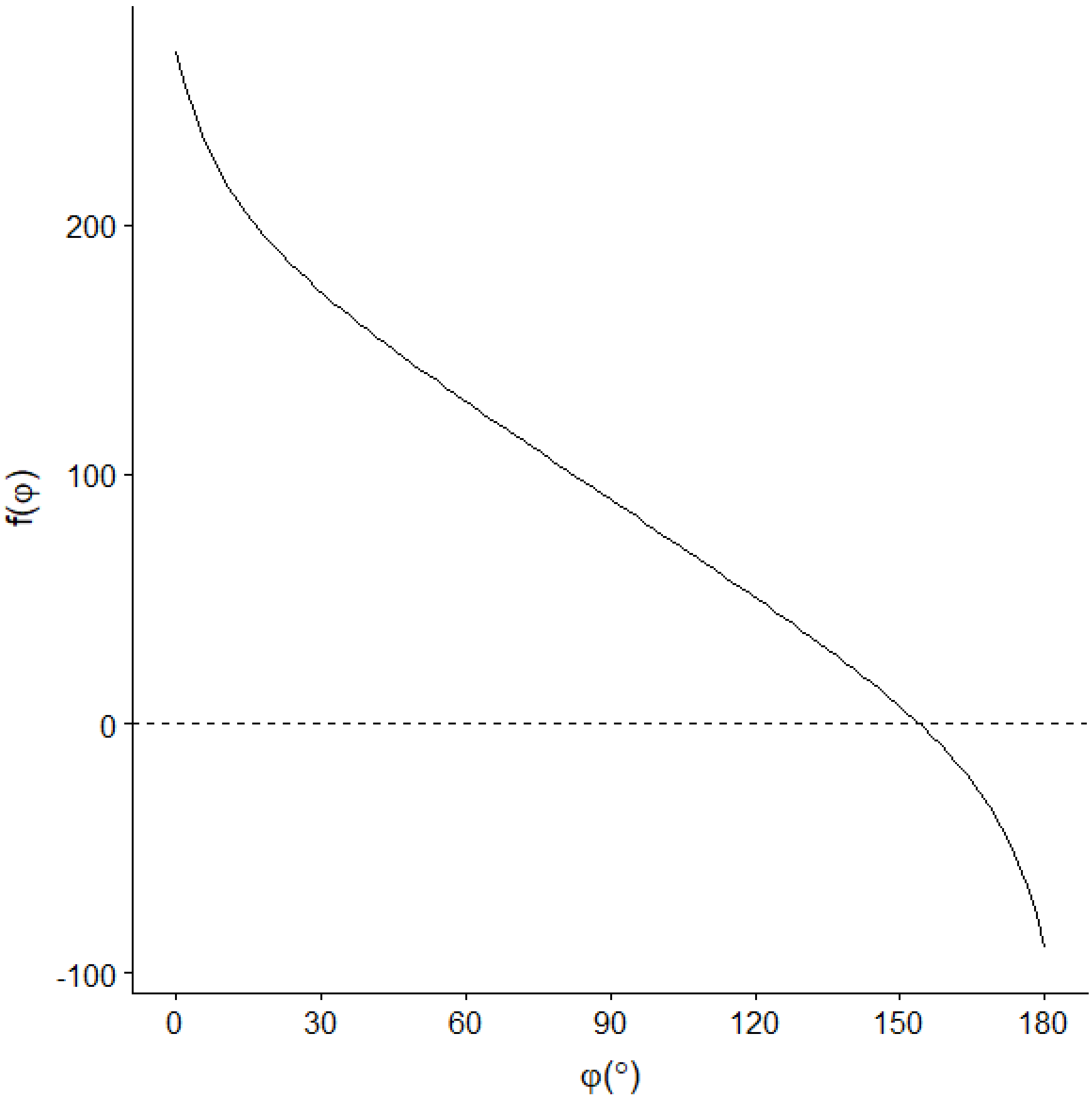

Figure 3.4. The plot of $f(\varphi)$ in the range of $0° < \varphi < 180°$. This plot is generated assuming following parameters: $\rho_o = 800\, kg/m^3$, $\rho_w = 1000\, kg/m^3$, $g = 9.8\, N/kg$, $R = 200\mu m$, $\sigma = 0.05\, N/m$, $\theta = 0°$ and $S_o = 0.5$.

3.3. PS Model of Interfacial Polarization Considering Wettability Effect

3.3.1. Surface area of graphite particle covered by water and oil

The surface area of graphite particle covered by water and oil can easily be calculated using equation for the curved surface area of a spherical cap. The surface area of graphite particle covered by water is:

$$A_w = 2\pi R^2 (1 - cos\,\varphi) \tag{19}$$

So, the proportion of graphite surface that covered by water is:

$$p_w = \frac{A_w}{A_s} = \frac{2\pi R^2 (1 - cos\,\varphi)}{4\pi R^2} = \frac{1 - cos\,\varphi}{2} \tag{20}$$

where A_s is the surface area of graphite particle.

The surface area of graphite particle covered by oil is:

$$A_o = 2\pi R^2 (1 + cos\,\varphi) \tag{21}$$

So, the proportion of graphite surface that covered by oil is:

$$p_o = \frac{A_o}{A_s} = \frac{2\pi R^2 (1 + cos\,\varphi)}{4\pi R^2} = \frac{1 + cos\,\varphi}{2} \tag{22}$$

3.3.2. PS model considering wettability effect

The previously discussed PS model is coupled with the new wettability model for wetting angle estimation, which accounts for the wettability of graphite and oil saturation:

$$\frac{\sigma_{eff}^* - \sigma_h^*}{\sigma_{eff}^* + 2\sigma_h^*} = \phi_g p_w f_{gw}(\omega) + \phi_g p_o f_{go}(\omega) + \phi_s f_s(\omega) + \phi_c f_c(\omega) + \phi_o f_o(\omega) \tag{23}$$

where $f_{gw}(\omega)$ and $f_{go}(\omega)$ is dipolarizability of graphite when host medium is water and oil, respectively. Note σ_h^* is the complex conductivity of host electrolyte, which is water.

3.3.3. Limitations

The small slope assumption for the determination of meniscus shape requires that the distance r < the capillary length L_c. If r > L_c, gravitational effects become significant and cause the interface height to decay exponentially (Cavallaro Jr, 2012). To meet the requirements of the Maxwell-Garnett effective medium formula, the volume fraction of nonconductive and conductive inclusions in the mixture should be less than 20% (Revil et al., 2015). For the purpose of petrophysical studies, the subsurface hydrocarbon-bearing reservoir rocks have less than 10% volume fraction of conductive mineral inclusions but the volume fraction of non-conductive particles possessing surface charge (e.g. clay and sand) can exceed 20%. Like other mixing theories, our model assumes that the magnitude of spatial variations of the electric field is smaller than the magnitude of variations in the intrinsic electrical properties and geometrical structures. Moreover, all calculations are performed using a quasi-static assumption that requires the size of heterogeneities to be much smaller than the wavelength of the applied EM field (Cosenza et al., 2009). Also, when dealing with a lossy medium, the skin depth of the EM wave must be considered to avoid strong attenuation of the field amplitudes in the conductive heterogeneities.

Moreover, in the derivation of dipolarizability, Poisson-Nernst-Planck (PNP) equation is invoked in the bulk electrolyte that introduces a decaying length scale, where the Maxwell-Garnett formula may become invalid at even lower concentration of inclusion phase (Hou et al., 2018). Also, a limitation of the PNP equations arises from the omission of the finite volume effect of charge carriers, mutual interactions and steric effects, effects due to transport of ions in confined channels of the pore system, and correlation effects (Chu and Bazant, 2006). Another limitation arises because the model is developed only for symmetric, and binary charge carriers in both the host and inclusion phases. This assumption simplifies the analytical complexity of the PNP formulations. Another drawback of the PNP equation is that the analysis is performed for materials that contain completely dissociated charge carriers at low concentration values. Moreover, in this thesis, unlike Chu and Bazant (2006), we only consider the linear response to weak fields where exact solutions are possible and are closer to the field conditions.

We also claim that the PPIP model is reliable for studying the EM response of mixtures containing uniformly distributed conductive particles of characteristic length a < 1 mm, conductivity σ_i < 10^5 S/m, relative permittivity $\varepsilon_{r,i}$ < 20, relative magnetic permeability equal to 1, and volume fraction ϕ_i < 20% in the frequency range of 100 Hz to 100 MHz. Beyond these limits, the PPIP model predictions will incur significant discrepancies with measurements due to the skin effect of the inclusion phase. The skin effect is primarily governed by the operating frequency and conductivity of the inclusion phase. PPIP model predictions are physically consistent only when the estimated skin depth is an order of magnitude larger than the characteristic length of the particles, where skin depth is defined by the depth from the surface till which alternating current flow in the conductive particle.

Chapter 4: Validations

In this section, the PS model predictions are compared with the published experimental data. The properties of mixtures used for generating plots are summarized in the corresponding tables, where ϕ_i is the volume fraction of a specific phase, a_i is the characteristic length (radius) of spherical particles, D is diffusion coefficient of charge carriers, ε_r is relative permittivity, σ is conductivity, and λ is surface conductance. Property of host medium and inclusion phase are represented with a subscript of h and i, respectively.

Schwan et al. (1962) conducted laboratory investigations of dielectric enhancement and dielectric dispersion of colloidal suspensions of polystyrene spheres of uniform size in an ionic electrolyte. Their experiments considered the frequency range from 10 Hz to several MHz. For modeling purposes, they used a frequency-dependent surface admittance circuit model to explain their laboratory measurements. In that paper, the authors mentioned the need to develop a mechanistic model to predict experimental data. Figure 4.1 compares the PS model predictions and experimental data from Schwan et al. (1962). PS model predictions are in good agreement with experimental results, for input values that are similar to published ones. Also, we obtain good agreement for the computed $\varepsilon_{r,eff}$ of the suspension with another set of experimental results mentioned in Schwan et al. (1962), as shown in Figure 4.2. Figures 4.1 and 4.2 imply that the presence of dispersed polystyrene particles produces drastic dielectric enhancement and dispersion due to interfacial polarization phenomena because neither the host nor the inclusion individually possesses dielectric characteristics comparable to that measured in the experiments. On the other hand, Figure 4.1 indicates relatively smaller conductivity dispersion in the order of 1% relative difference between the high- and low-frequency values of conductivity, which is attributed to the absence of high-mobility charge carriers in the inclusion phase.

Table 4.1. The known, assumed and estimated properties used for generating Figure 4.1

Property		Known	Assumed	Estimated
Inclusion (polystyrene particles)	ϕ_i (%)	30		
	a_i (µm)	0.094		
	$\varepsilon_{r,i}$		2.5	
	λ (S)			6.7×10^{-9}
Host (KCl solution)	D_h (m^2/s)		1.6×10^{-9}	
	$\varepsilon_{r,h}$		78	
	σ_h (S/m)			0.348

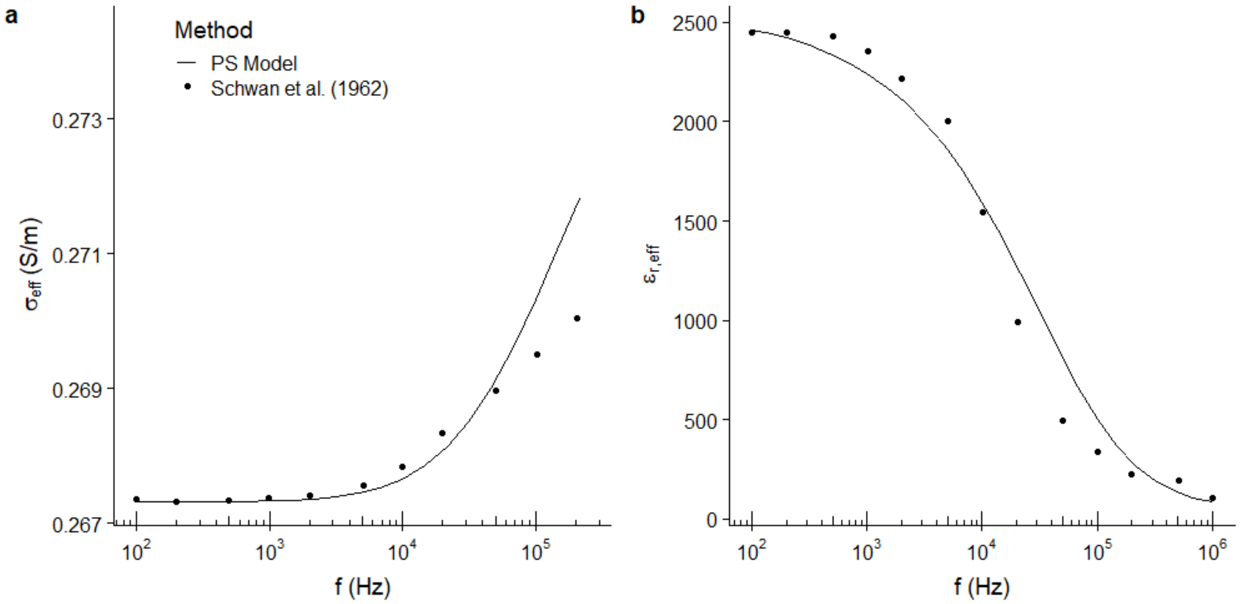

Figure 4.1. Comparison of the PS model predictions of (a) σ_{eff} and (b) $\varepsilon_{r,eff}$ against that measured by Schwan et al. (1962). The properties used for generating this plot is shown in Table 4.1.

Table 4.2. The known, assumed and estimated properties used for generating Figure 4.2

Property		Known	Assumed	Estimated
Inclusion (polystyrene particles)	ϕ_i (%)	19.5		
	a_i (µm)	0.2785		
	$\varepsilon_{r,i}$		2.5	
	λ (S)			6×10^{-9}
Host (KCl solution)	D_h (m^2/s)			1×10^{-9}
	$\varepsilon_{r,h}$		78	
	σ_h (S/m)	0.125		

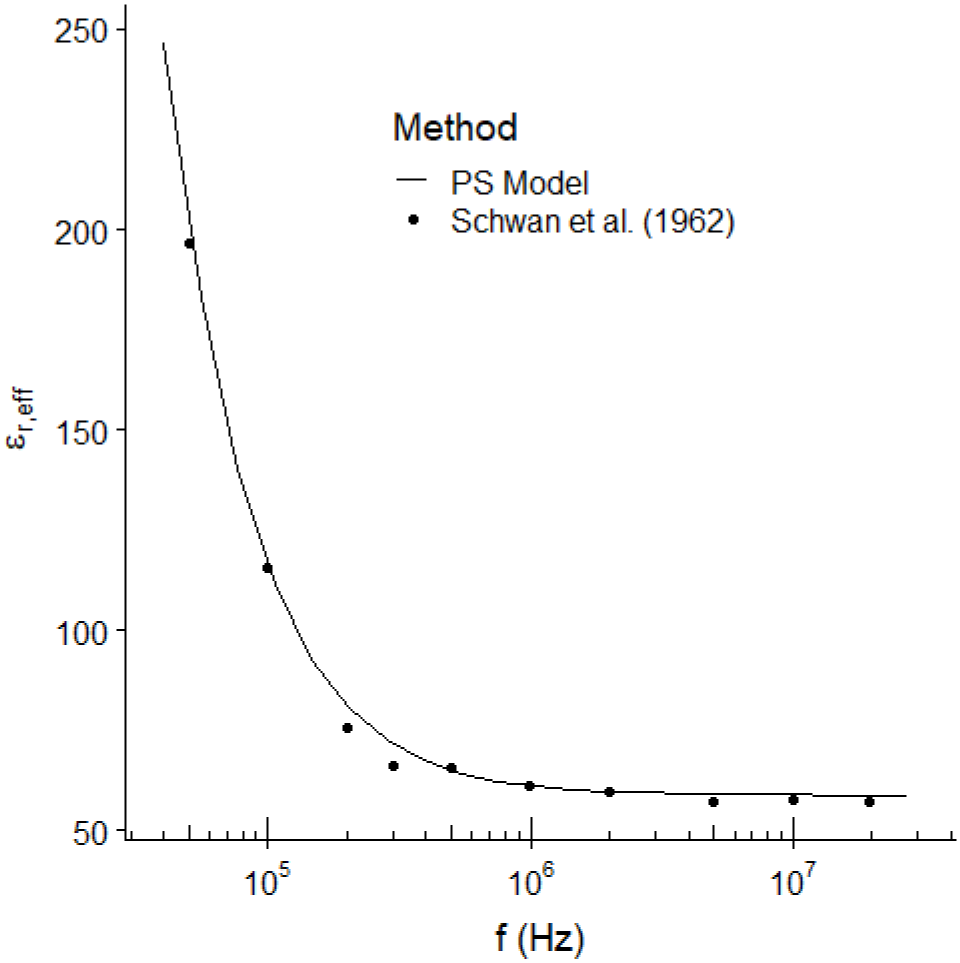

Figure 4.2. Comparison of the PS model predictions of $\varepsilon_{r,eff}$ against that measured by Schwan et al. (1962). The properties used for generating this plot is shown in Table 4.2.

Tirado and Grosse (2006) performed broadband dielectric measurements on suspensions of spherical polystyrene particles having high surface charge distribution in an aqueous solution. Interfacial polarization phenomena in their experiment is dominated by surface conductance effects due to high surface charge of polystyrene particles. Figure 4.3 shows a good agreement between Tirado and Grosse's (2006) measurements and the PS model predictions.

Table 4.3. The known, assumed and estimated properties used for generating Figure 4.3

Property		Known	Assumed	Estimated
Inclusion (polystyrene particles)	ϕ_i (%)	1		
	a_i (µm)	0.5		
	$\varepsilon_{r,i}$		2	
	λ (S)			9×10^{-9}
Host (KCl solution)	D_h (m^2/s)	2×10^{-9}		
	$\varepsilon_{r,h}$		80	
	σ_h (S/m)	0.00554		

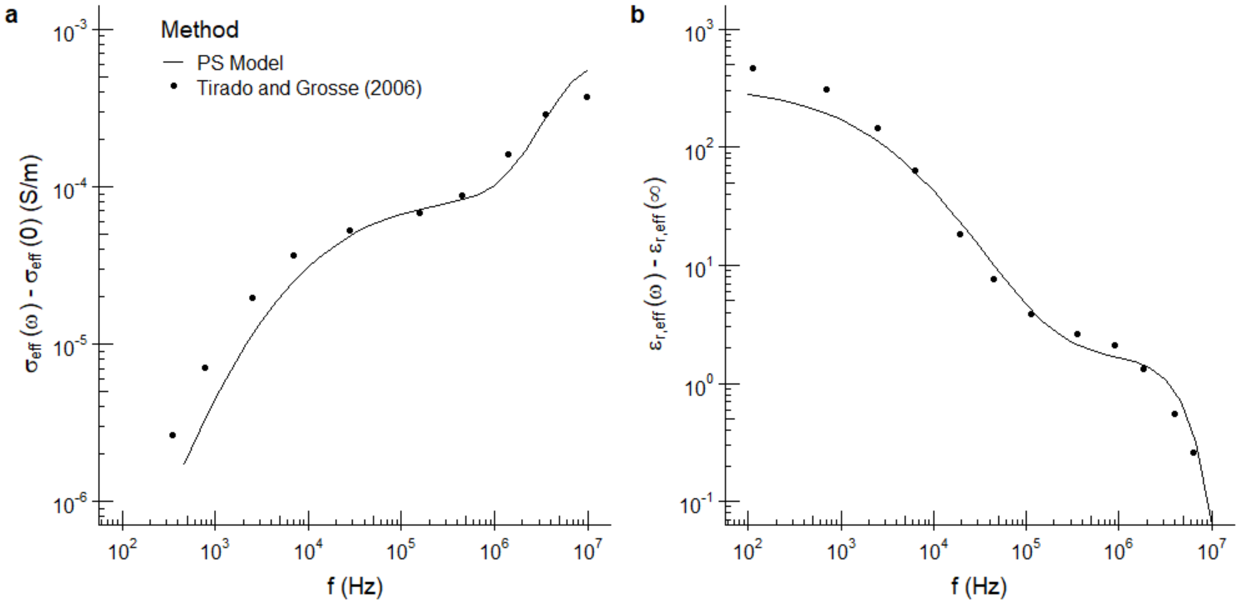

Figure 4.3. Comparison of the PS model predictions of (a) change of effective conductivity ($\sigma_{eff}(\omega) - \sigma_{eff}(0)$) and (b) change of effective relative permittivity ($\varepsilon_{r,eff}(\omega) - \varepsilon_{r,eff}(\infty)$)

against that measured by Tirado and Grosse (2006). The properties used for generating this plot is shown in Table 4.3.

Further, we modeled experiments performed by Delgado et al. (1998), who worked on identifying laboratory techniques to differentiate surface diffusion mechanism from the volume diffusion mechanism. They carried out dielectric dispersion measurements on suspensions of polymer latex balls in a KCl solution. PS modeling results matched experimental results for two different volume fractions of polymer latex balls in a KCl solution, as shown in Figure 4.4.

Table 4.4. The known, assumed and estimated properties used for generating Figure 4.4

Property		Known	Assumed	Estimated
Inclusion (polymer latex balls)	ϕ_i (%)	15.6 or 12.7		
	a_i (nm)	55		
	$\varepsilon_{r,i}$		5	
	λ (S)			2.8×10^{-10}
Host (KCl solution)	D_h (m^2/s)			2.3×10^{-10}
	$\varepsilon_{r,h}$		78	
	σ_h (S/m)		0.0147	

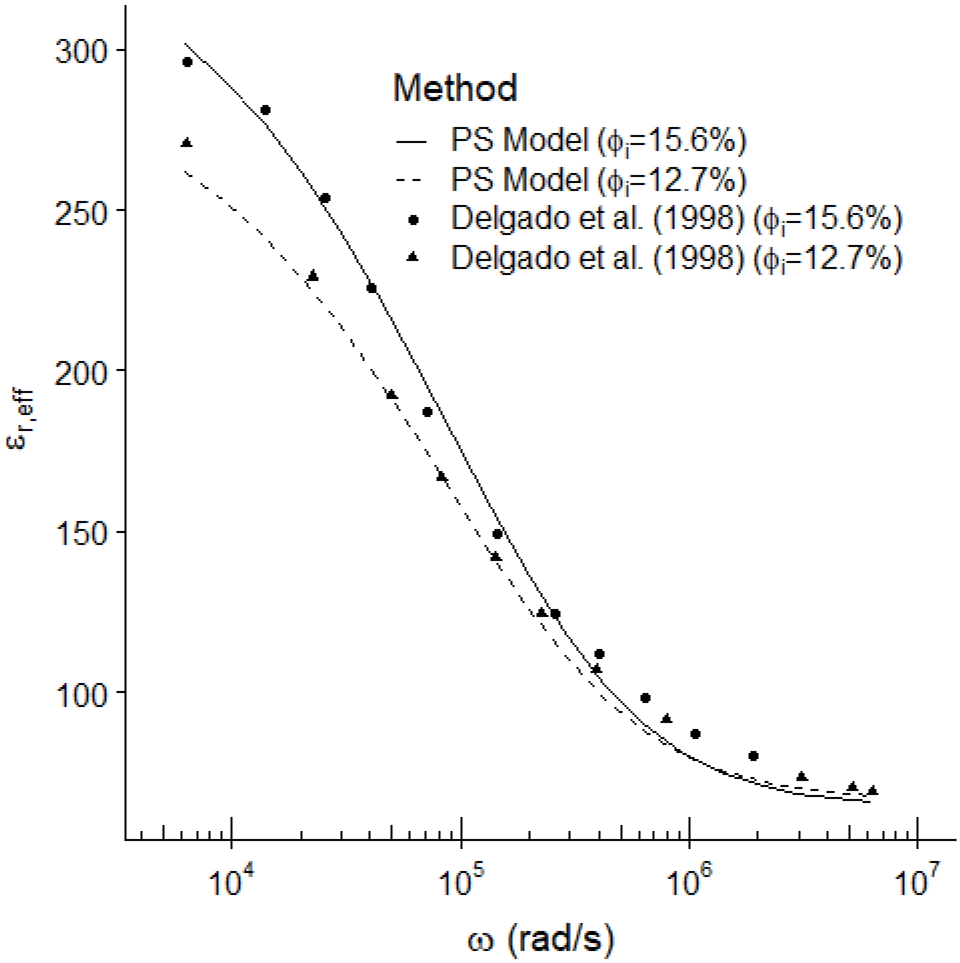

Figure 4.4. Comparison of the PS model predictions of $\varepsilon_{r,eff}$ against that measured by Delgado et al. (1998). The properties used for generating this plot is shown in Table 4.4.

Chapter 5: Results and Discussions

5.1. Sensitivity of PS Model

In this section, the effects of PPIP and SCAIP phenomena on low-frequency (100 Hz) σ_{eff} and high-frequency (1 GHz) $\varepsilon_{r,eff}$ predictions are evaluated. The properties of mixtures used for generating plots are summarized in the corresponding tables, where ϕ_i is the volume fraction of a specific phase, a_i is the characteristic length (radius) of spherical particles, D is diffusion coefficient of charge carriers, ε_r is relative permittivity, σ is conductivity, and λ is surface conductance. Property of host medium and inclusion phase are represented with a subscript of h and i, respectively.

5.1.1. PS model sensitivity to the properties of the nonconductive spherical particles

In this section, we investigate the sensitivity of the PS model predictions of σ_{eff} and $\varepsilon_{r,eff}$ to the properties of surface-charge-bearing nonconductive particles. In Figure 5.1, curves S1 and S2 are pure sand with different volume fractions, which act as the references. Comparing curves S1 against S2, we conclude that the increase in volume fraction of nonconductive particles like sand grains will decrease the σ_{eff} and $\varepsilon_{r,eff}$. Comparing curves S1C4 and S1C5 against S1C1, the decrease of the characteristic length or the increase of the surface conductance of clay particles by two orders of magnitude leads to slight decrease in the σ_{eff} and increase the $\varepsilon_{r,eff}$, as shown in Figure 5.1a and 5.1b, respectively. Moreover, for our model, mixture S1C2 and S1C3 gives the same prediction value for both σ_{eff} and $\varepsilon_{r,eff}$ because the clay particles in both mixtures have the same a_i/λ value and the same relative permittivity. It can also be observed that with the variation in frequency there are negligible dispersion effects on σ_{eff} and $\varepsilon_{r,eff}$.

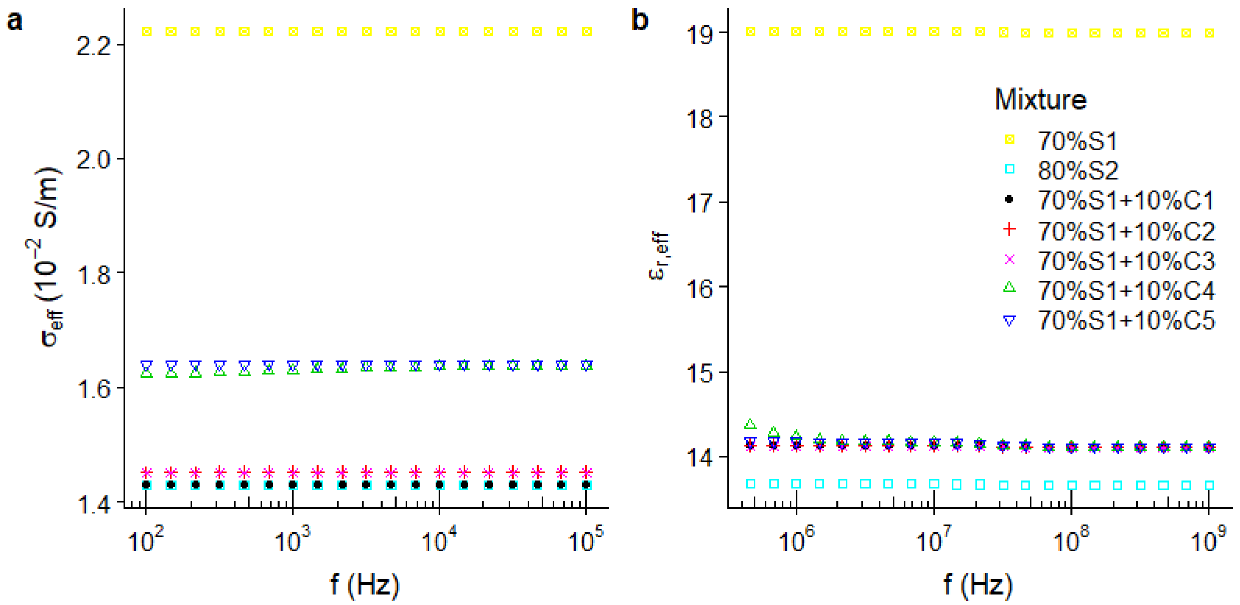

Figure 5.1. Effect of nonconductive particles. This figure shows a comparison of the PS model predictions for different properties of the nonconductive spherical particles. The mixtures contain nonconductive spherical sand particles and various types of clay particles (properties listed in Table 5.1) fully saturated with electrolyte of $\varepsilon_{r,h}$ of 70, σ_h of 0.1 S/m, and D_h of 10^{-9} m^2/s.

Table 5.1. Properties used for generating Figure 5.1, where S1 and S2 represent sand, and C1, C2, and C3 represent three different clay types, and the host is an electrolyte of $\varepsilon_{r,h}$ of 70, σ_h of 0.1 S/m, and D_h of 10^{-9} m^2/s. Typical ε_r of sand and clay ranges from 3 to 5 and 5 to 40, respectively (Martinez and Brynes, 2001). In this thesis, we assume ε_r of 4 for sand and 8 for clay.

	ϕ_i (%)	a_i (μm)	$\varepsilon_{r,i}$	λ (S)	a_i/λ
Sand1 (S1)	70	1000	4	10^{-9}	10^{12}
Sand2 (S2)	80	1000	4	10^{-9}	10^{12}
Clay1 (C1)	10	100	8	10^{-8}	10^{10}
Clay2 (C2)	10	10	8	10^{-8}	10^{9}
Clay3 (C3)	10	100	8	10^{-7}	10^{9}
Clay4 (C4)	10	1	8	10^{-8}	10^{8}
Clay5 (C5)	10	100	8	10^{-6}	10^{8}

5.1.2. PS model sensitivity to the properties of the conductive spherical particles

The mixtures studied in Figure 5.2 contain 70% volume fraction of sand and 10% volume fraction of uniformly distributed pyrite. In comparison with the reference curve S1, we can conclude that the presence of conductive particles will increase the $\varepsilon_{r,eff}$ and decrease σ_{eff} at low frequency but will increase σ_{eff} at high frequency. The results show that a higher relative permittivity or conductivity of conductive inclusions, like mixture S1P2 or S1P4, increases σ_{eff} and decreases $\varepsilon_{r,eff}$ of mixture, while a mixture with higher diffusion coefficient like S1P3 decreases σ_{eff} and increases $\varepsilon_{r,eff}$. Moreover, for our model, mixtures S1P1 and S1P5 gives the same prediction for both σ_{eff} and $\varepsilon_{r,eff}$ because both mixtures have the same σ/D value and the same ε_r. Mixture S1P2 and S1P4 also gives the same prediction for both σ_{eff} and $\varepsilon_{r,eff}$ because both mixtures have the same $\sigma\varepsilon_r$ and D. It's also worth to notice that the variation in σ_{eff} prediction only occurs for frequency between 1 kHz and 100 kHz, while the variation in $\varepsilon_{r,eff}$ prediction only occurs for frequency lower than about 5 MHz.

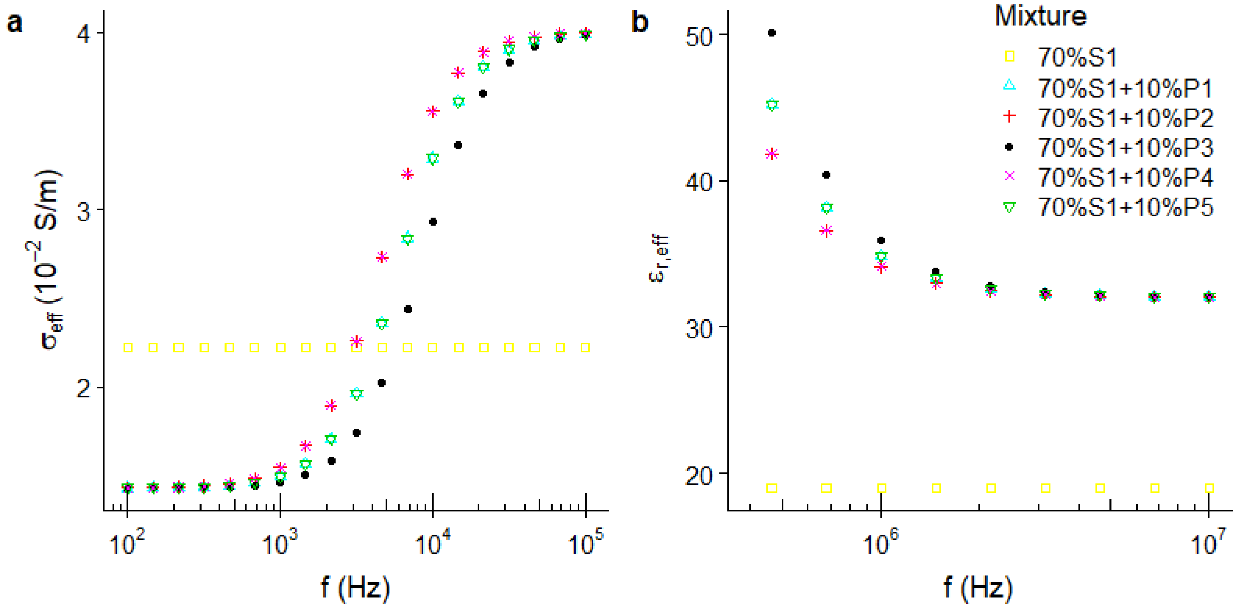

Figure 5.2. Effect of conductive particles. This figure shows a comparison of the PS model predictions for different properties of the conductive spherical particles. The mixtures contain surface-charge-bearing nonconductive spherical sand particles and various types of conductive spherical pyrite particles (properties listed in Table 5.2) fully saturated with electrolyte of $\varepsilon_{r,h}$ of 70, σ_h of 0.1 S/m and D_h of 10^{-9} m^2/s. Characteristic length of pyrite and sand particles is assumed to be 200 μm and 1000 μm, and the surface conductance λ of the sand is 10^{-9} S.

Table 5.2. Properties used for generating Figure 5.2, where S1 represents sand, P1 ~ P5 represent five different pyrite types, and the host is an electrolyte of $\varepsilon_{r,h}$ of 70, σ_h of 0.1 S/m and D_h of 10^{-9} m^2/s.

	ϕ_i (%)	D_i (m^2/s)	$\varepsilon_{r,i}$	σ_i (S/m)	σ_i/D_i	$\sigma_i\varepsilon_{r,i}$
Sand (S1)	70	-	4	-	-	-
Pyrite1 (P1)	10	5×10^{-5}	12	500	10^7	6×10^3
Pyrite2 (P2)	10	5×10^{-5}	24	500	10^7	1.2×10^4
Pyrite3 (P3)	10	10^{-4}	12	500	5×10^6	6×10^3
Pyrite4 (P4)	10	5×10^{-5}	12	1000	2×10^7	1.2×10^4
Pyrite5 (P5)	10	10^{-4}	12	1000	10^7	1.2×10^4

5.1.3. PS model sensitivity to the mixture of conductive and nonconductive spherical particles

In this section, the PS model predictions of complex conductivity for mixtures containing both nonconductive and conductive inclusions/particles are evaluated. The resulting plots are shown as Figure 5.3. Curve S1 act as reference curve representing a clean mixture of sand and electrolyte without any clay and pyrite particles. The presence of uniformly distributed surface-charge-bearing nonconductive and conductive inclusion phases will decrease the σ_{eff} to a value lower than that of clean formation at low frequency (Figure 5.3a). This is because at low frequency, the charge carriers quickly reach the equilibrium distribution around the interfaces under the influence of a time-varying electric field, so that the polarized conductive and nonconductive particles act as insulators due to the interface that does not allow charge migration, and hence the reduction in the net electromagnetic energy transport. For frequencies over 1 kHz, the σ_{eff} increases as frequency increases, which will become higher than that of the clean mixture if the frequency is high enough. σ_{eff} saturates for frequencies over 100 kHz. The presence of both nonconductive and conductive inclusion phases will increase the $\varepsilon_{r,eff}$ (Figure 5.3b) because the PPIP and SCAIP phenomena leads to larger charge accumulation around the interfaces, and hence higher net electromagnetic energy storage. The $\varepsilon_{r,eff}$ decreases as frequency increases and become stable for frequencies over around 5 MHz. When both conductive and nonconductive spherical inclusions exist in the mixture, the effect of nonconductive inclusions are negligible compared to that of conductive inclusions, which is illustrated by the overlap of S1C1P1 and S1C2P1. In other words, the physical properties of conductive inclusions dominate the predictions.

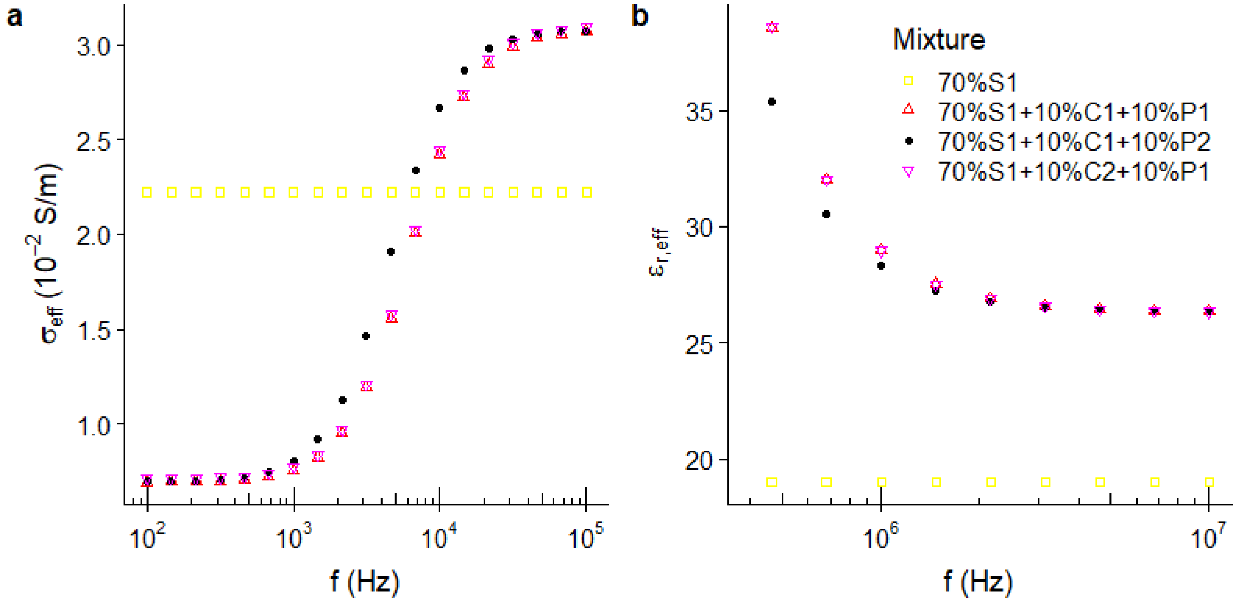

Figure 5.3. Effect of the mixture of conductive and nonconductive particles. This figure shows a comparison of the PS model predictions for different properties of the mixture of conductive and nonconductive spherical particles. The mixtures contain nonconductive spherical sand particles, various types of clay particles, and various types of conductive spherical pyrite particles (properties listed in Table 5.3) fully saturated with electrolyte of $\varepsilon_{r,h}$ of 70, σ_h of 0.1 S/m and D_h of 10^{-9} m^2/s.

Table 5.3. Properties used for generating Figure 5.3, where S1 represents sand, C1 and C2 represent two different clay types, and P1 and P2 represent two different pyrite types. The host is an electrolyte of $\varepsilon_{r,h}$ of 70, σ_h of 0.1 S/m, and D_h of 10^{-9} m^2/s.

	ϕ_i (%)	a_i (μm)	D_i (m^2/s)	$\varepsilon_{r,i}$	σ_i (S/m)	λ (S)
Sand (S1)	70	1000	-	4	-	10^{-9}
Clay1 (C1)	10	100	-	8	-	10^{-8}
Clay2 (C2)	10	100	-	8	-	10^{-7}
Pyrite1 (P1)	10	200	5×10^{-5}	12	500	-
Pyrite2 (P2)	10	200	5×10^{-5}	12	1000	-

5.1.4. PS model sensitivity to the characteristic lengths of particles

In this section, the PS model predictions of complex conductivity for mixtures containing both nonconductive and conductive inclusions/particles of various sizes are evaluated. The resulting plots are shown as Figure 5.4. Curve S1 is the reference curve. The characteristic length of surface-charge-bearing nonconductive particle seems have little effect on model predictions when both conductive and nonconductive particles are present in the mixture (as observed from the overlap between S1C1P1 and S1C2P1). For conductive inclusions, a smaller characteristic length will shift the frequency dispersion of σ_{eff} and $\varepsilon_{r,eff}$ response to higher frequencies (i.e. shift the curves towards right in both the plots). Therefore, σ_{eff} reduces and $\varepsilon_{r,eff}$ increases for mixtures containing conductive particles of smaller characteristic lengths.

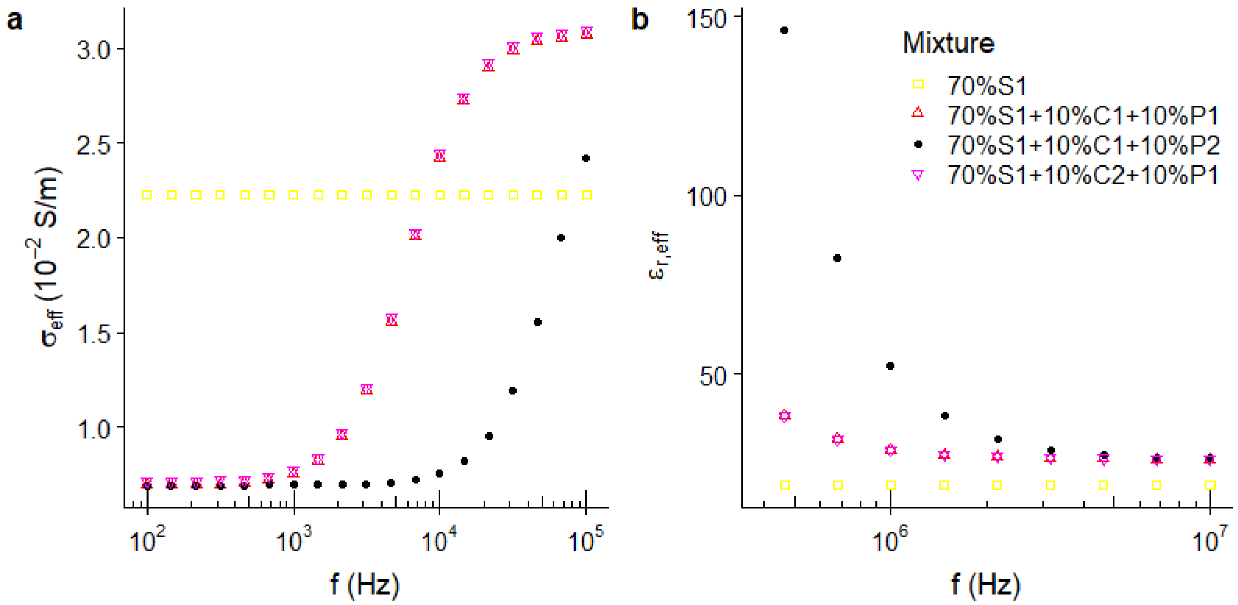

Figure 5.4. Effect of the characteristic lengths of particles. This figure shows a comparison of the PS model predictions for different characteristic lengths of particles. The mixtures contain spherical sand, clay and pyrite particles of various sizes (properties listed in Table 5.4) and fully saturated with electrolyte of $\varepsilon_{r,h}$ of 70, σ_h of 0.1 S/m and D_h of 10^{-9} m^2/s.

Table 5.4. Properties used for generating Figure 5.4, where S1 represents sand, C1 and C2 represent two different clay types, and P1 and P2 represent two different pyrite types and the host is an electrolyte of $\varepsilon_{r,h}$ of 70, σ_h of 0.1 S/m and D_h of 10^{-9} m^2/s.

	ϕ_i (%)	a_i (μm)	D_i (m^2/s)	$\varepsilon_{r,i}$	σ_i (S/m)	λ (S)
Sand (S1)	70	1000	-	4	-	10^{-9}
Clay1 (C1)	10	100	-	8	-	10^{-8}
Clay2 (C2)	10	10	-	8	-	10^{-8}
Pyrite1 (P1)	10	200	5×10^{-5}	12	500	-
Pyrite2 (P2)	10	20	5×10^{-5}	12	500	-

5.1.5. PS model sensitivity to the volume fractions of particles

The effects of volume fraction of nonconductive and conductive particles are evaluated in this section. Figure 5.5 shows the result, where Curve S1 is the reference curve. Comparing S1C1P1, S1C2P1 and S1C1P2 curves in Figure 5.5a, an increase in volume fraction of surface-charge-bearing nonconductive particles increases the magnitude of the frequency dispersion of σ_{eff} due to the increase in the net polarization effect; this appears as a downward shift. On the other hand, an increase in the volume fraction of conductive particles, causes a steep rise (a high rate of increase) in the frequency dispersion of σ_{eff}. For frequencies lower than 1kHz, σ_{eff} values are constant. Comparison of S1C1P1, S1C2P1 and S1C1P2 curves in Figure 5.5b indicates an increase in the volume fraction of nonconductive particles shifts the frequency dispersion curve of $\varepsilon_{r,eff}$ to lower values, while an increase in volume fraction of conductive particles shifts the curve to much larger values.

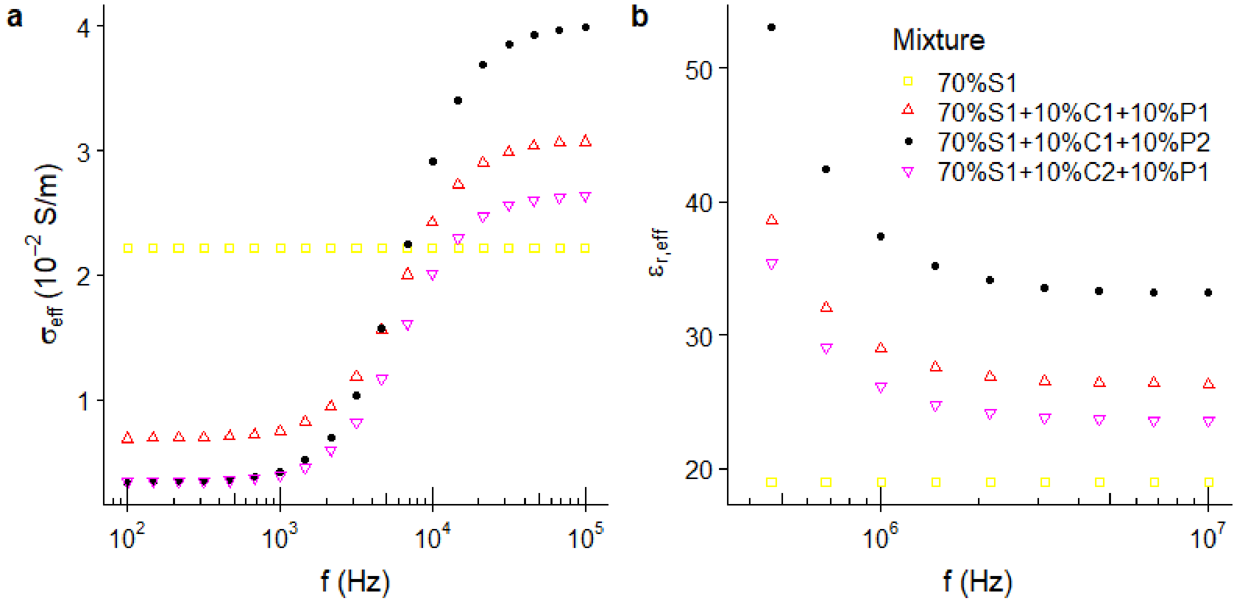

Figure 5.5. Effect of the volume fractions of particles. This figure shows a comparison of the PS model predictions for different volume fractions of particles. The mixtures contain spherical sand, clay and pyrite particles at various volume fractions of the inclusion phase (Table 5.5) and fully saturated with electrolyte of $\varepsilon_{r,h}$ of 70, σ_h of 0.1 S/m and D_h of 10^{-9} m^2/s.

Table 5.5. Properties used for generating Figure 5.5, where S1 represents sand, C1 and C2 represent clay with different volume fractions, and P1 and P2 represent pyrite with different volume fractions and the host is an electrolyte of $\varepsilon_{r,h}$ of 70, σ_h of 0.1 S/m and D_h of 10^{-9} m^2/s.

	ϕ_i (%)	a_i (μm)	D_i (m^2/s)	$\varepsilon_{r,i}$	σ_i (S/m)	λ (S)
Sand (S1)	70	1000	-	4	-	10^{-9}
Clay1 (C1)	10	100	-	8	-	10^{-8}
Clay2 (C2)	15	100	-	8	-	10^{-8}
Pyrite1 (P1)	10	200	5×10^{-5}	12	500	-
Pyrite2 (P2)	15	200	5×10^{-5}	12	500	-

5.1.6. PS model sensitivity to the conductivity of pore-filling electrolyte

The effects of conductivity of electrolyte are evaluated in this section. As for σ_{eff} prediction, we can clearly observe that the increase of electrolyte conductivity shifts the dispersion to higher frequencies (right shift). The low-frequency dispersion can hardly be observed for electrolyte with conductivity value higher than 1 S/m (Figure 5.6c). When the electrolyte conductivity is increased by one order of magnitude, the corresponding σ_{eff} prediction also increases by one order of magnitude, similar to Archie's law. As for $\varepsilon_{r,eff}$ prediction, it can also be concluded that $\varepsilon_{r,eff}$ is positively related to the conductivity of electrolyte because a greater charge carrier concentration in electrolyte leads to greater charge accumulation around the interface. Moreover, the conductive particles dominate the prediction of $\varepsilon_{r,eff}$ for frequencies below 5 MHz, especially with the conductivity of the electrolyte is high.

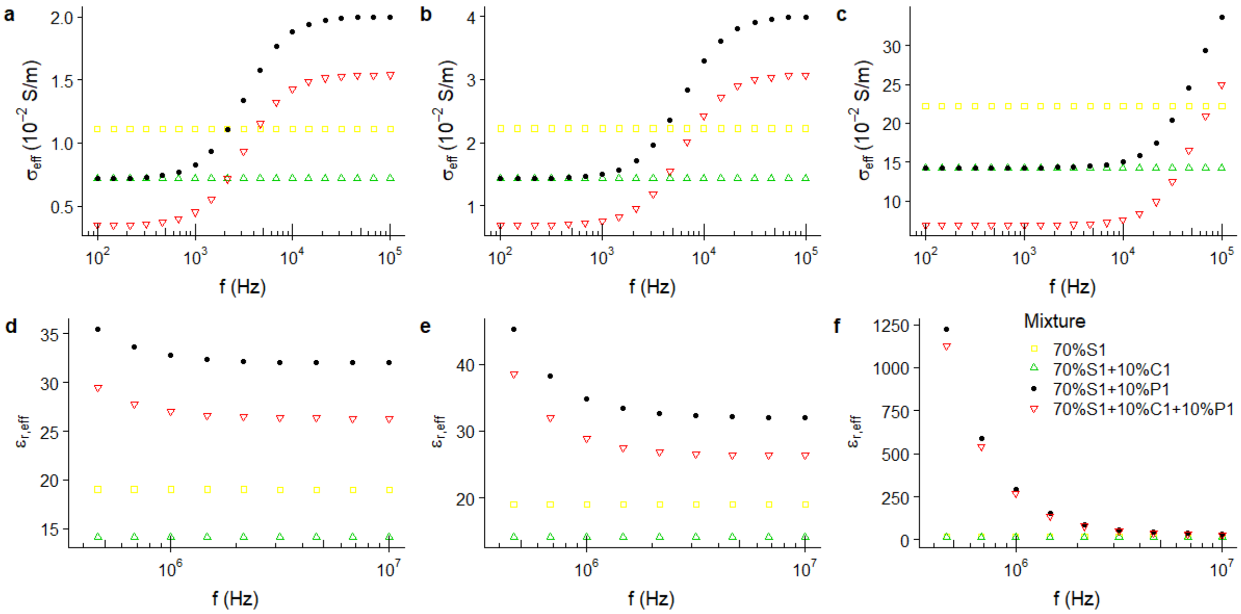

Figure 5.6. Effect of the conductivities of electrolyte. This figure shows a comparison of the PS model predictions for different conductivities of pore-filling electrolyte. The mixtures contain spherical sand, clay and pyrite particles (properties listed in Table 5.6) and fully saturated with electrolyte of various conductivity σ_h, $\varepsilon_{r,h}$ of 70, and D_h of 10^{-9} m^2/s. (a), (b), (c) represent σ_{eff} prediction, and (d), (e), (f) represent $\varepsilon_{r,eff}$ prediction for mixtures fully saturated with 0.05, 0.1, and 1 S/m electrolyte, respectively.

Table 5.6. Properties used for generating Figure 5.6, where S1 represents sand, C1 represents clay, and P1 represents pyrite and the host is an electrolyte of $\varepsilon_{r,h}$ of 70 and D_h of 10^{-9} m^2/s.

	ϕ_i (%)	a_i (μm)	D_i (m^2/s)	$\varepsilon_{r,i}$	σ_i (S/m)	λ (S)
Sand (S1)	70	1000	-	4	-	10^{-9}
Clay (C1)	10	100	-	8	-	10^{-8}
Pyrite (P1)	10	200	5×10^{-5}	12	500	-

5.1.7. PS model sensitivity to the volume fractions of oil

In this thesis, we model oil as nonconductive spherical droplets of specific size (100 μm) uniformly distributed in the mixture, so the effect of increase in oil saturation can be seen as that of increase in the volume fraction of a nonconductive spherical particle with unique properties, as described in Table 5.7. Comparing the curves with reference curve S1, we conclude that the increase in volume fraction of oil will decrease the σ_{eff} and $\varepsilon_{r,eff}$.

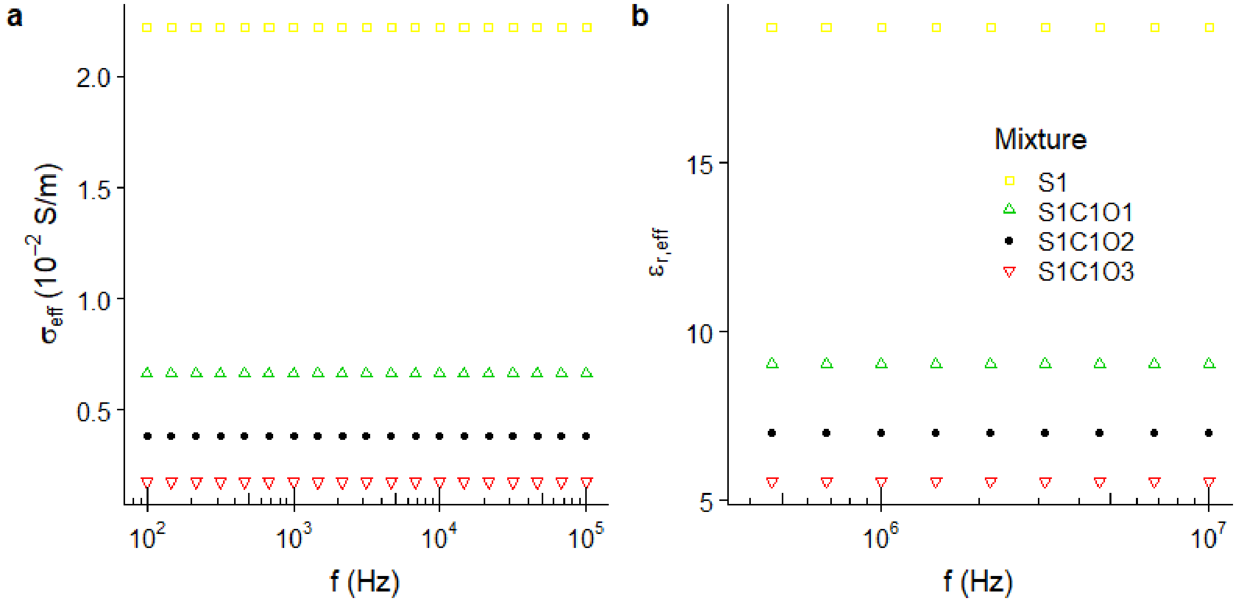

Figure 5.7. Effect of the volume fractions of oil. This figure shows a comparison of the PS model predictions for different volume fractions of oil. The mixtures contain spherical sand, clay and pyrite particles partially saturated with electrolyte of $\varepsilon_{r,h}$ of 70, σ_h of 0.1 S/m and D_h of 10^{-9} m^2/s and containing different volume fractions of oil. The properties of sand, clay, pyrite and oil are

listed in Table 7. O1~O3 represent oil volume fractions of 1%, 5% and 8% (which correspond to oil saturation of 5%, 25% and 40%, respectively, if porosity is 20%).

Table 5.7. Properties used for generating Figure 5.7, where S1 represents sand, C1 represents clay, and O1~O3 represent different volume fractions of oil. The host is an electrolyte of $\varepsilon_{r,h}$ of 70, σ_h of 0.1 S/m and D_h of 10^{-9} m^2/s.

	ϕ_i (%)	a_i (μm)	D_i (m^2/s)	$\varepsilon_{r,i}$	σ_i (S/m)	λ (S)
Sand (S1)	70	1000	-	4	-	10^{-9}
Clay (C1)	20	10	-	8	-	10^{-8}
Oil (O1~3)	1, 5, 8	100	-	2	-	10^{-30}

5.2. Sensitivity of PS Model Considering Wettability Effect

The effect of wettability of graphite particle and oil saturation on effective conductivity (σ_{eff}) and effective relative permittivity ($\varepsilon_{r,eff}$) prediction of the mixture in the frequency range of 100Hz ~ 10MHz is evaluated. The properties of host mediums and inclusions used for generating the plots are summarized in the corresponding tables, where σ is interfacial tension between oil and water, ϕ_i is the volume fraction of a specific phase, a_i is the characteristic length (radius) of spherical particles, D_j is diffusion coefficient of charge carriers, $\varepsilon_{r,j}$ is relative permittivity, σ_j is conductivity, and λ is surface conductance. The subscript j takes the form of i for the inclusion phase and h for the host phase. In this paper, oil is both inclusion phase (for the effect on electrical properties prediction) and host phase (for the effect on graphite wettability). We also assume the sand and clay particles are fully water wet.

5.2.1. PS model sensitivity to the contact angle of spherical graphite particles

In this section, we investigate the sensitivity of PS model predictions of σ_{eff} and $\varepsilon_{r,eff}$ to the contact angle of spherical graphite particle. Compare the different curves in Figure 5.8 (a & c) or Figure 5.8 (b & d), we can see the frequency dispersion reduces as contact angle increases. Because as contact angle increases, graphite surface is covered more by oil, which has much less charge carriers than water. Compare Figure 5.8 (a & c) and Figure 5.8 (b & d), the increase of oil saturation will also reduce the frequency dispersion because the graphite surface is covered more by oil, similar to the effect of contact angle. The details on the influence of oil saturation will be discussed in the next section. Note as oil saturation increases, both σ_{eff} and $\varepsilon_{r,eff}$ will reduce due to the increase in the volume fraction of oil as nonconductive inclusion (Jin et al., 2019). Both σ_{eff} and $\varepsilon_{r,eff}$ will converge to a single value at high frequency, due to the charge carriers move rapidly and there is no net accumulation around particles. In this case, the electrical properties are only affected by conductivity of host electrolyte and volume fractions of conductive or surface-charge-bearing nonconductive inclusions (Jin et al., 2019). In contrast, at low frequency, the charge carriers quickly reach the equilibrium distribution around the particles' interface, so that the polarized particles act as insulators, which lead to lower σ_{eff} and higher $\varepsilon_{r,eff}$ (Jin et al., 2019).

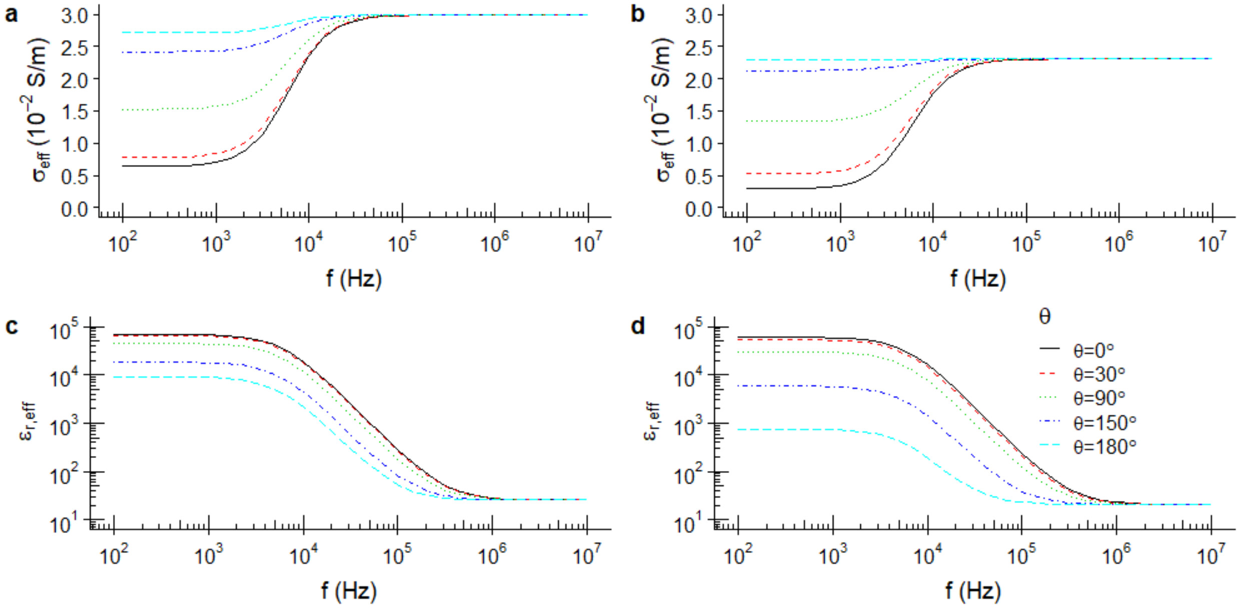

Figure 5.8. Effect of the contact angles of graphite. This figure shows a comparison of the PS model predictions for different contact angles of spherical graphite particles. The mixture contain graphite with various contact angles (0° ~ 180°), sand and clay particles partially saturated with electrolyte and containing 1% (a & c) or 9% (b & d) volume fractions of oil (which correspond to oil saturation of 10% and 90%, respectively, given 10% porosity we assumed for this figure). The properties of host mediums are listed in Table 5.8. The properties of graphite, sand, clay and oil as inclusion are listed in Table 5.9.

Table 5.8. Properties of host mediums.

	D_h (m^2/s)	$\varepsilon_{r,h}$	σ_h (S/m)	ρ_h (kg/m^3)	σ (N/m)
Water	10^{-9}	70	0.1	1000	0.05
Oil	10^{-15}	2	10^{-30}	800	

Table 5.9. Properties of inclusions used for generating Figure 5.8.

	ϕ_i (%)	a_i (μm)	D_i (m^2/s)	$\varepsilon_{r,i}$	σ_i (S/m)	λ (S)	θ (°)
Graphite	10	200	5×10^{-5}	12	500	-	0 ~ 180
Sand	70	1000	-	4	-	10^{-9}	-
Clay	10	100	-	8	-	10^{-8}	-
Oil	1 or 9	100	-	2	-	10^{-30}	-

5.2.2. PS model sensitivity to the oil saturation of the mixture

In this section, we investigate the sensitivity of PS model predictions of σ_{eff} and $\varepsilon_{r,eff}$ to the oil saturation of the mixture. Compare the different curves in Figure 5.9 (a & d), Figure 5.9 (b & e) or Figure 5.9 (c & f), we can see the frequency dispersion reduces as oil saturation increases because graphite surface is covered more by oil, similar to the effect of contact angle. Keep in mind that as oil saturation increases, both σ_{eff} and $\varepsilon_{r,eff}$ will reduce due to the increase in the volume fraction of oil as nonconductive inclusion (Jin et al., 2019). Also, by comparing the rate of change among curves in Figure 5.8 (a & c) and Figure 5.9 (a & d), we can conclude that in our model, the effect of oil saturation is less than the effect of contact angle (i.e. the contact angle plays a primary effect and oil saturation plays a secondary effect).

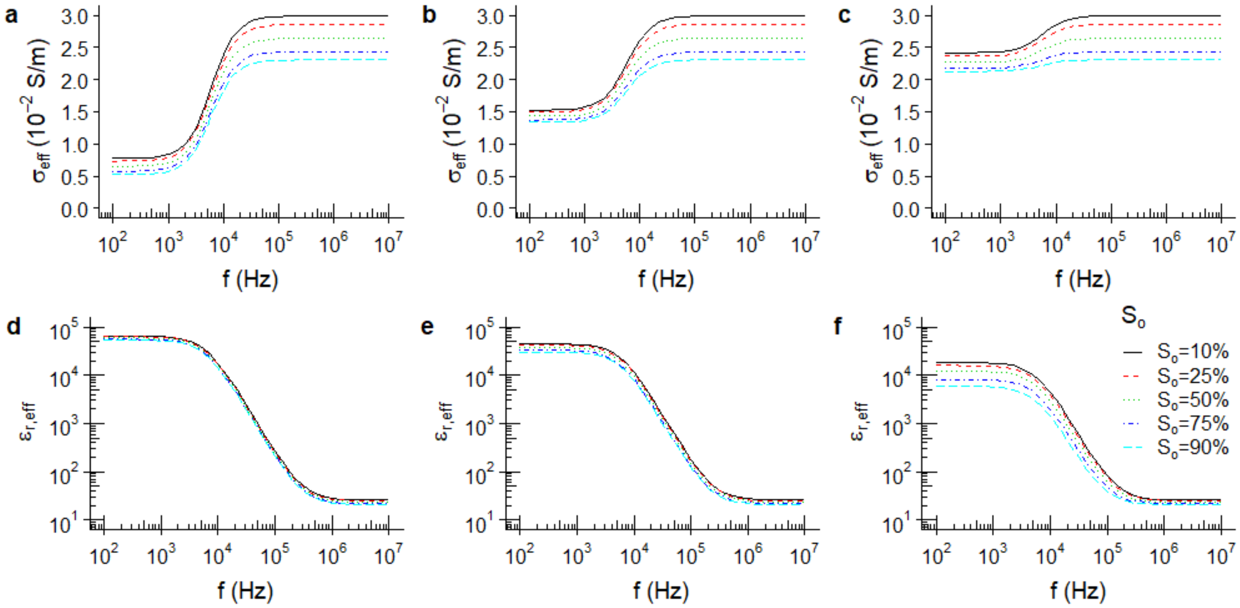

Figure 5.9. Effect of the oil saturations of the mixture. This figure shows a comparison of the PS model predictions for different oil saturations of the mixture. The mixtures contain graphite with contact angles of 30° (a & d), 90° (b & e) or 150° (c & f), sand and clay particles partially saturated with electrolyte and containing various volume fractions of oil. The properties of host mediums are listed in Table 5.8 above. The properties of graphite, sand, clay and oil as inclusion are listed in Table 5.10. Oil volume fractions of 1%, 2.5%, 5%, 7.5% and 9% corresponds to oil saturations of 10%, 25% 50%, 75% and 90%, respectively, given 10% porosity we assumed for this figure.

Table 5.10. Properties of inclusions used for generating Figure 5.9.

	ϕ_i (%)	a_i (μm)	D_i (m^2/s)	$\varepsilon_{r,i}$	σ_i (S/m)	λ (S)	θ (°)
Graphite	10	200	5×10^{-5}	12	500	-	30, 90 or 150
Sand	70	1000	-	4	-	10^{-9}	-
Clay	10	100	-	8	-	10^{-8}	-
Oil	1 ~ 9	100	-	2	-	10^{-30}	-

5.2.3. PS model sensitivity to the volume fraction of water-wet and oil-wet graphite

In this section, we investigate the sensitivity of PS model predictions of σ_{eff} and $\varepsilon_{r,eff}$ to the volume fraction of water-wet and oil-wet graphite. We set the total volume fraction of graphite particles to 10%. Figure 5.10 shows that as we gradually decrease the volume fraction of water-wet graphite while increasing that of oil-wet graphite, the frequency dispersion reduces because more graphite surface is covered by oil, as we discussed before.

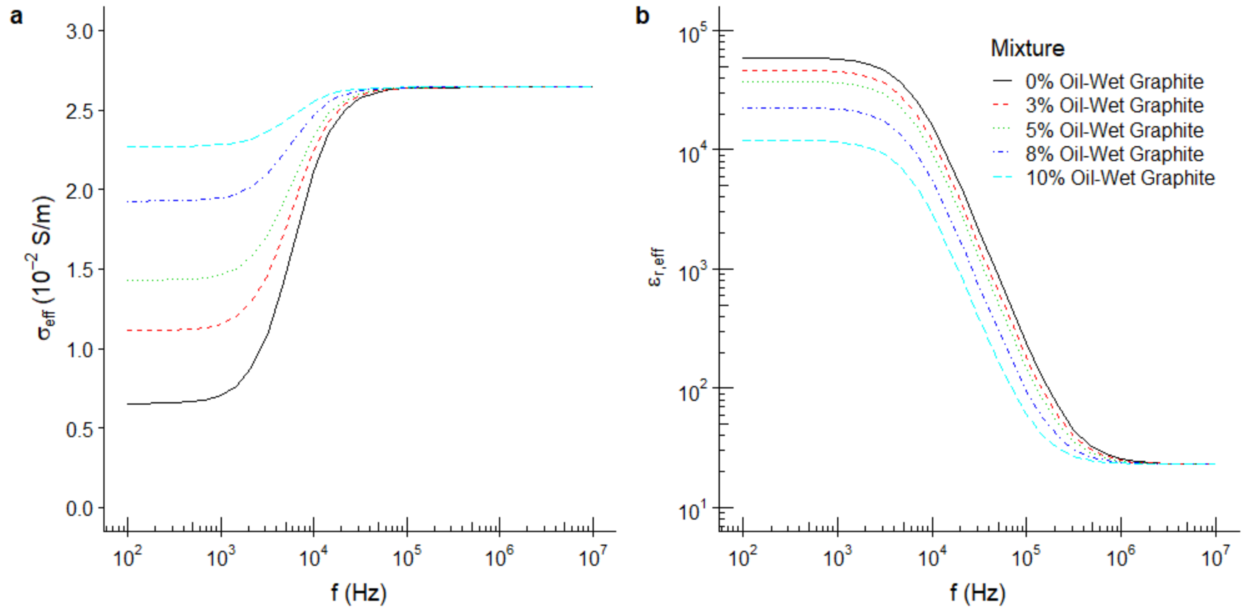

Figure 5.10. Effect of the volume fractions of water-wet and oil-wet graphite. This figure shows a comparison of the PS model predictions for different volume fractions of water-wet and oil-wet graphite. The mixtures contain various volume fractions of water-wet graphite with contact angle of 30° (Graphite 1), various volume fractions of oil-wet graphite with contact angle of 150° (Graphite 2), sand and clay particles partially saturated with electrolyte and containing 5% volume fraction of oil (which correspond to oil saturation of 50% given 10% porosity we assumed for this figure). The total volume fraction of graphite is 10%. The properties of host mediums are listed in Table 5.8 above. The properties of graphite, sand, clay and oil as inclusion are listed in Table 5.11.

Table 5.11. Properties of inclusions used for generating Figure 5.10.

	ϕ_i (%)	a_i (μm)	D_i (m^2/s)	$\varepsilon_{r,i}$	σ_i (S/m)	λ (S)	θ (°)
Graphite 1	0 ~ 10	200	5×10^{-5}	12	500	-	30
Graphite 2	10 ~ 0	200	5×10^{-5}	12	500	-	150
Sand	70	1000	-	4	-	10^{-9}	-
Clay	10	100	-	8	-	10^{-8}	-
Oil	5	100	-	2	-	10^{-30}	-

Chapter 6: Application of MCMC Inversion Method to Estimate Contact Angle and Oil Saturation

Formation evaluation in conventional reservoirs always involves the estimation of subsurface petrophysical properties such as oil saturation, which can be interpreted from EM log measurements. However, the EM log interpretations are more complicated when dealing with unconventional reservoirs. Several inversion methods are proposed which are coupled with subsurface characterization models to estimate such petrophysical parameters. Han and Misra (2018) developed a modified Levenberg- Marquardt algorithm-based inversion method coupled with PS model to jointly perform petrophysical interpretation of EM log data. Also, the Markov chain Monte Carlo (MCMC) inversion method can be applied to the improved PS model to estimate model parameters of interest like oil saturation, contact angle or conductivity of brine using the electromagnetic log measurements (Han et al., 2019). Compared to deterministic inversion methods such as Gauss-Newton method or Levenberg-Marquardt method which are gradient-based least-squares approach and sensitive to initial guess, the MCMC sampling-based stochastic method is a global approach for parameter estimation and able to quantify the uncertainty of the unknown petrophysical parameters (Chen et al., 2008).

To illustrate the application of MCMC inversion method for estimating petrophysical parameters, we process two sets of synthetic EM broadband dispersion log data of synthetic hydrocarbon-bearing formation containing mixed-wet graphite and sand to estimate oil saturation and contact angle of graphite. Assume synthetic layer 1 contains water-wet graphite and synthetic layer 2 contains oil-wet graphite. The properties of host mediums are summarized in Table 6.1 and the properties of inclusions of the mixtures are summarized in Table 6.2. The synthetic EM log responses are generated by the above-mentioned PS model using parameters in Table 6.1 and 6.2 as input for 5 frequencies: 26 kHz, 20 MHz, 100 MHz, 260 MHz and 1 GHz. 5% Gaussian noise is added to the synthetic log response. For the two synthetic layers, oil saturation S_o and contact angle θ are the two petrophysical parameters to be estimated using the inversion algorithm.

Table 6.1. Properties of host mediums of synthetic layers

	D_h (m^2/s)	$\varepsilon_{r,h}$	σ_h (S/m)	ρ_h (kg/m^3)	σ (N/m)
Water	10^{-9}	70	0.1	1000	0.05
Oil	10^{-15}	2	10^{-30}	800	

Table 6.2. Properties of inclusions of synthetic layers

	ϕ_i (%)	a_i (μm)	D_i (m^2/s)	$\varepsilon_{r,i}$	σ_i (S/m)	λ (S)	θ (°)
Graphite	10	200	5×10^{-5}	12	500	-	30 or 120
Sand	80	1000	-	4	-	10^{-9}	-
Oil	8 (S_o=80%)	100	-	2	-	10^{-30}	-

To perform MCMC inversion, we need to define the prior ranges and initial values of petrophysical parameters for the Markov chains, which is shown in Table 6.3. The prior ranges of the petrophysical parameters constrain the boundary of the parameters in the model space.

Table 6.3. Prior ranges and initial values of petrophysical parameters for the Markov chains

Parameter	Prior Range	Initial Value 1	Initial Value 2	Initial Value 3
S_o (%)	(0, 100)	80	40	10
θ (°)	(0, 180)	30	90	150

We use three Markov chains staring at different initial guesses when inverting the synthetic broadband frequency EM log data. The inversion history of the three Markov chains is shown in Figure 6.1 and 6.2. The use of three Markov chain starting at different initial values can help to detect possible local convergence (Chen et al., 2008). The inversion processes converge after about 300 iterations for the two synthetic layers.

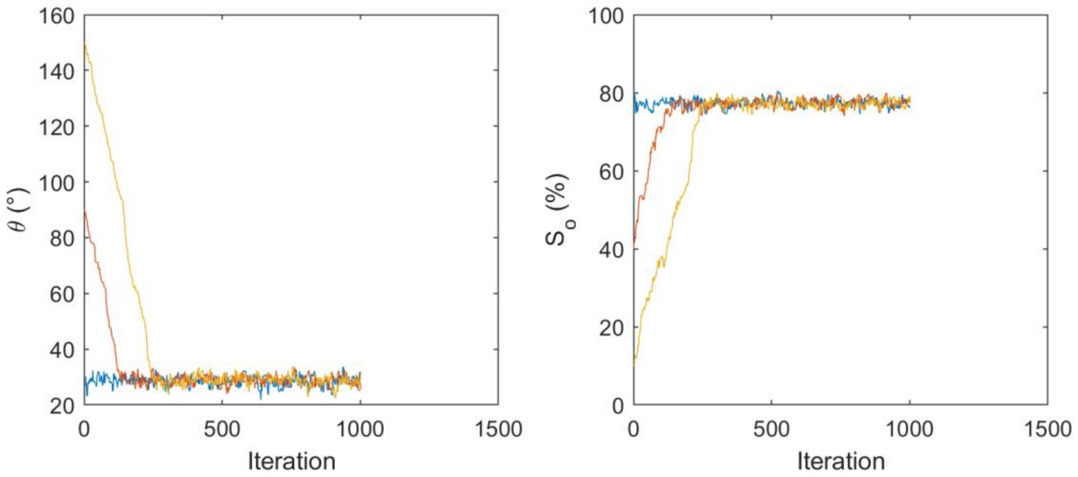

Figure 6.1. Inversion history for synthetic layer 1

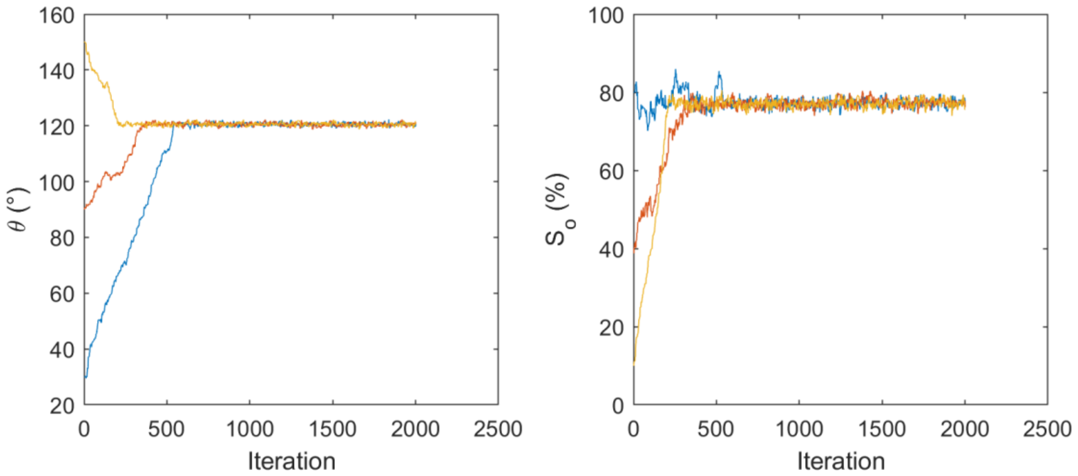

Figure 6.2. Inversion history for synthetic layer 2

All the samples in the second half of each Markov chain are used to generate the histograms of the estimated petrophysical parameters, as shown in Figure 6.3 and 6.4. And the inversion results for the two synthetic mixtures are summarized in Table 6.4. The estimated Highest Posterior Density (HPD) interval for the parameters are close to the real values. Also, the model prediction using the estimated petrophysical values are compared with the true values, as shown in Figure 6.5 and 6.6. We can see a good match between the true values and modeled values. We conclude that the MCMC inversion is robust to noise and the estimated parameters are close to pre-defined synthetic values.

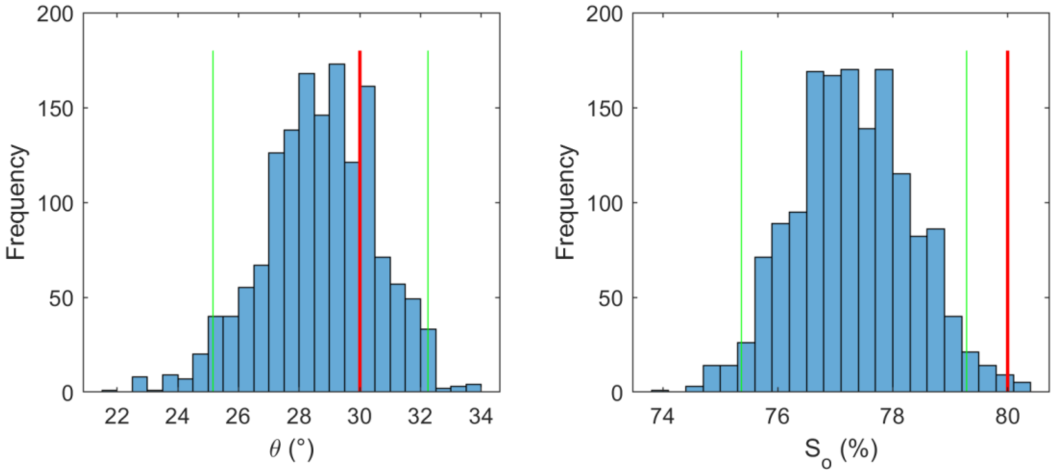

Figure 6.3. Histograms of Estimated Parameters for synthetic layer 1. The red line represents true value and green lines represent 95% HPD Interval.

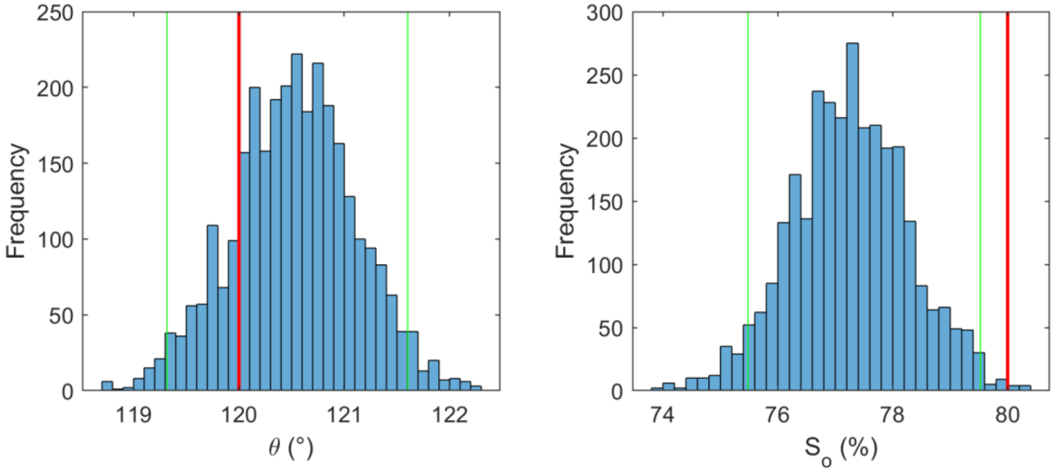

Figure 6.4. Histograms of Estimated Parameters for synthetic layer 2. The red line represents true value and green lines represent 95% HPD Interval.

Table 6.4. Inversion results for the two synthetic layers

		S_o (%)	θ (°)
Synthetic mixture 1	True value	80	30
	95% HPD Interval	(75.4, 79.3)	(25.2, 32.2)
Synthetic mixture 2	True value	80	120
	95% HPD Interval	(75.5, 79.5)	(119.3, 121.6)

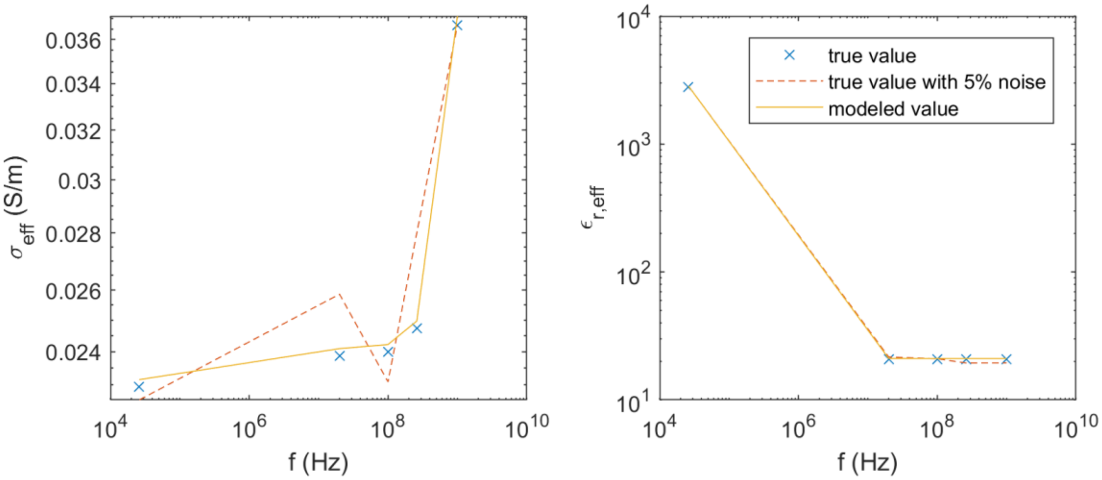

Figure 6.5. Comparison between model prediction using estimated parameters and true values for synthetic layer 1

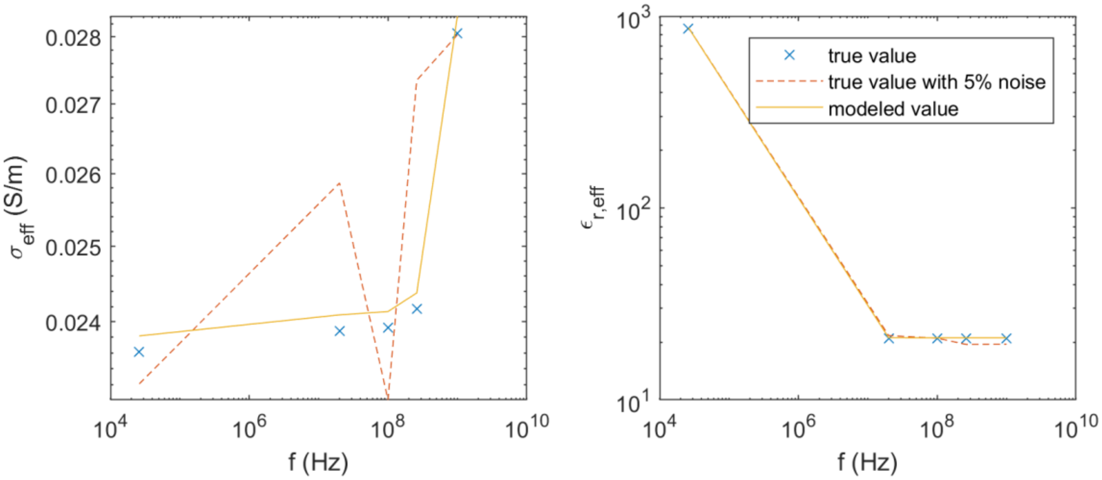

Figure 6.6. Comparison between model prediction using estimated parameters and true values for synthetic layer 1

Chapter 7: Conclusions

We developed a mechanistic model of multi-frequency complex conductivity for a homogeneous, oil/water-filled, porous geomaterial containing surface-charge-bearing non-conductive particles (e.g. clay and sand grains) and conductive mineral particles (e.g. pyrite and graphite particles). The mechanistic model accounts for the interfacial polarization (IFP) effects due to the surface conductance of water-wet clays and that due to the conductive particles of any wettability at any oil saturation.

We studied the IFP effects of clays and conductive minerals on the effective conductivity (σ_{eff}) in the frequency range of 100 Hz to 100 kHz and on the effective permittivity ($\varepsilon_{r,eff}$) in the frequency range of 0.5 MHz to 1 GHz. A decrease in size or an increase in the surface conductance of surface-charge-bearing nonconductive particles, referred herein as clays, uniformly distributed in a porous homogeneous mixture leads to a slight decrease in the σ_{eff} and an increase in the $\varepsilon_{r,eff}$. Clay particles with the same ratio of size to surface conductance and the same relative permittivity (ε_r) have the same effects on the complex conductivity. In the frequency windows mentioned above, the frequency dispersions of complex conductivity due to the IFP effects for clays are negligible compared to conductive particles.

The presence of conductive particles increases the $\varepsilon_{r,eff}$ and decreases the σ_{eff} at lower frequencies. A higher relative permittivity or conductivity of conductive particles increases σ_{eff} and decreases $\varepsilon_{r,eff}$ of mixture, whereas a higher diffusion coefficient of conductive particles decreases σ_{eff} and increases $\varepsilon_{r,eff}$. Conductive particles with the same ratio of particle conductivity to diffusion coefficient and the same ε_r or those with the same value of conductivity times permittivity and diffusion coefficient have the same effects on the complex conductivity of the mixture. For conductive inclusions, a smaller particle size shifts the frequency dispersion of σ_{eff} and $\varepsilon_{r,eff}$ responses to higher frequencies. Therefore, σ_{eff} reduces and $\varepsilon_{r,eff}$ increases for mixtures containing conductive particles of smaller characteristic lengths. For the conductive particles studied in this paper, the frequency dispersion in σ_{eff} occurs for frequency between 1 kHz and 100 kHz, whereas the dispersion in $\varepsilon_{r,eff}$ occurs for frequency lower than about 5 MHz.

An increase in volume fraction of surface-charge-bearing nonconductive particles increases the magnitude of the frequency dispersion of σ_{eff} due to the increase in the net polarization effect; this appears as a reduction in σ_{eff}. On the other hand, an increase in the volume fraction of conductive particles, causes a steep rise (a high rate of increase) in the frequency dispersion of σ_{eff}. An increase in the volume fraction of nonconductive particles slightly decreases $\varepsilon_{r,eff}$, while an increase in volume fraction of conductive particles increases the values by around 20%. An increase in brine conductivity shifts the dispersion of σ_{eff} prediction to higher frequencies. When the brine conductivity is increased by one order of magnitude, the corresponding σ_{eff} prediction also increases by one order of magnitude, similar to Archie's law. The low-frequency dispersion can hardly be observed for electrolyte with conductivity value higher than 1 S/m. $\varepsilon_{r,eff}$ is positively related to the conductivity of electrolyte because a greater charge carrier concentration in electrolyte leads to greater charge accumulation around the interface. Moreover, the conductive particles dominate the prediction of $\varepsilon_{r,eff}$ for frequencies below 5 MHz, especially when the conductivity of the electrolyte is high.

We also developed a novel mechanistic model to quantify the effects of wettability of conductive particles on the multi-frequency complex conductivity of fluid-filled porous materials, which involves solving Young-Laplace equation to determine the spreading of oil and water phase around the conductive particles. We studied the effect of wettability of graphite particle and oil saturation on σ_{eff} and effective relative permittivity $\varepsilon_{r,eff}$ prediction of the mixture in the frequency range of 100Hz ~ 10MHz.

Wettability effects of conductive particles cannot be neglected when dealing with conductivity and permittivity measurements at low frequencies, especially at high oil saturations. However, wettability effects are negligible when dealing with conductivity and permittivity measurements at frequencies greater than 0.1 MHz and 1 MHz, respectively. Frequency dispersions of conductivity and permittivity increases with increase in water wetness of the conductive particle. As water wetness of conductive particles increases, the low-frequency conductivity decreases because more charge carriers are involved in the charge polarization and accumulation as compared to charge transport. Contrary to low-frequency conductivity, high-frequency conductivity is less sensitive to contact angle of the conductive particle as compared to the oil saturation. Also, compared to low-frequency permittivity, high-frequency permittivity is much less sensitive to oil saturation. The effect of oil saturation is less than the effect of contact angle on the frequency dependence of conductivity and permittivity (i.e. the contact angle plays a primary effect and oil saturation plays a secondary effect).

Markov chain Monte Carlo (MCMC) inversion method is coupled with the PS model to process the multifrequency electromagnetic logs/measurements at five frequencies to estimate oil saturation and contact angle. The estimated parameters and the 95% HPD intervals are obtained for the synthetic data. The MCMC inversion is robust to noise and the estimated parameters are close to pre-defined synthetic values.

References

[1] Al-Ofi SM, Dyshlyuk E, Sauerer B, Valori A, Ali F, Abdallah W. Correlating Dielectric Dispersion Data and Wettability Index of a Carbonate Rock. In SPE Kingdom of Saudi Arabia Annual Technical Symposium and Exhibition 2018 Aug 16. Society of Petroleum Engineers.

[2] Altman R, Anderson B, Rasmus J, Lüling MG. Dielectric effects and resistivity dispersion on induction and propagation-resistivity logs in complex volcanic lithologies: A case study. In: 49th Annual Logging Symposium 2008 Jan 1. Society of Petrophysicists and Well-Log Analysts.

[3] Anderson BI, Barber TD, Lüling MG, Rasmus J, Sen PN, Tabanou JR, Haugland M. Observations of large dielectric effects on LWD propagation-resistivity logs. In: 48th Annual Logging Symposium 2007 Jan 1. Society of Petrophysicists and Well-Log Analysts.

[4] Bona N, Ortenzi A, Capaccioli S. Advances in understanding the relationship between rock wettability and high-frequency dielectric response. Journal of Petroleum Science and Engineering. 2002 Apr 1;33(1-3):87-99.

[5] Bona N, Rossi E, Capaccioli S. Electrical Measurements in the 100Hz-10GHz for Efficient Rock Wettability Evaluation. InSPE International Symposium on Oilfield Chemistry 1999 (pp. 50720-1). Society of Petroleum Engineers.

[6] Bona N, Rossi E, Venturini C, Capaccioli S, Lucchesi M, Rolla PA. Characterization of rock wettability though dielectric measurements. Revue de l'Institut Français du Pétrole. 1998 Nov 1;53(6):771-83.

[7] Bustin RM, Ross JV, Rouzaud JN. Mechanisms of graphite formation from kerogen: experimental evidence. International Journal of Coal Geology. 1995 Oct 1;28(1):1-36.

[8] Capaccioli S, Lucchesi M, Casalini R, Rolla PA, Bona N. Influence of the wettability on the electrical response of microporous systems. Journal of Physics D: Applied Physics. 2000 May 7;33(9):1036.

[9] Cavallaro Jr M. Assembly of rod-like particles at fluid interfaces. The Johns Hopkins University; 2012.

[10] Chakarov DV, Oesterlund L, Kasemo B. Water adsorption and coadsorption with potassium on graphite (0001). Langmuir. 1995 Apr;11(4):1201-14.

[11] Chen J, Kemna A, Hubbard SS. A comparison between Gauss-Newton and Markov-chain Monte Carlo–based methods for inverting spectral induced-polarization data for Cole-Cole parameters. Geophysics. 2008 Nov 14;73(6):F247-59.

[12] Chu KT, Bazant MZ. Nonlinear electrochemical relaxation around conductors. Physical Review E. 2006 Jul 6;74(1):011501.

[13] Clark TH. The origin of graphite. Economic Geology. 1921 Apr 1;16(3):167-83.

[14] Clavier C, Heim A, Scala C. Effect of pyrite on resistivity and other logging measurements. In: SPWLA 17th Annual Logging Symposium 1976 Jan 1. Society of Petrophysicists and Well-Log Analysts.

[15] Corley B, Garcia A, Maurer HM, Rabinovich MB, Zhou Z, DuBois P, Shaw Jr N. Study of unusual responses from multiple resistivity tools in the Bossier formation of the Haynesville shale play. In: SPE Annual Technical Conference and Exhibition 2010 Jan 1. Society of Petroleum Engineers.

[16] Cosenza P, Ghorbani A, Camerlynck C, Rejiba F, Guérin R, Tabbagh A. Effective medium theories for modelling the relationships between electromagnetic properties and

hydrological variables in geomaterials: a review. Near Surface Geophysics. 2009 Oct 1;7(5-6):563-78.

[17] Crain ER. Crain's petrophysical handbook. Spectrum 2000 Mindware Limited; 2002.

[18] Delgado AV, Arroyo FJ, González-Caballero F, Shilov VN, Borkovskaya YB. The effect of the concentration of dispersed particles on the mechanisms of low-frequency dielectric dispersion (LFDD) in colloidal suspensions. Colloids and Surfaces A: Physicochemical and Engineering Aspects. 1998 Sep 30;140(1-3):139-49.

[19] Deng Y, Shi X, Revil A, Wu J, Ghorbani A. Complex conductivity of oil-contaminated clayey soils. Journal of Hydrology. 2018 Jun 1;561:930-42.

[20] Dukhin SS, Shilov VN, Bikerman JJ. Dielectric phenomena and double layer in disperse systems and polyelectrolytes. Journal of the Electrochemical Society. 1974 Apr 1;121(4):154C-.

[21] Fiegel J, Jin F, Hanes J, Stebe K. Wetting of a particle in a thin film. Journal of colloid and interface science. 2005 Nov 15;291(2):507-14.

[22] Freed DE, Seleznev N, Hou CY, Fellah K, Little J, Dumy G, Sen P. A Physics-Based Model for the Dielectric Response of Shaly Sands and Continuous CEC Logging. Petrophysics. 2018 Jun 1;59(03):354-72.

[23] Garcia A, Barchini R, Grosse C. The influence of diffusion on the permittivity of a suspension of spherical particles with insulating shells in an electrolyte. Journal of Physics D: Applied Physics. 1985 Sep 14;18(9):1891.

[24] Garrouch AA, Sharma MM. The influence of clay content, salinity, stress, and wettability on the dielectric properties of brine-saturated rocks: 10 Hz to 10 MHz. Geophysics. 1994 Jun;59(6):909-17.

[25] Giordano S. Effective medium theory for dispersions of dielectric ellipsoids. Journal of electrostatics. 2003 May 1;58(1-2):59-76.

[26] Grosse C, Barchini R. The influence of diffusion on the dielectric properties of suspensions of conductive spherical particles in an electrolyte. Journal of Physics D: Applied Physics. 1992 Mar 14;25(3):508.

[27] Grosse C. Permittivity of a suspension of charged spherical particles in electrolyte solution. 2. Influence of the surface conductivity and asymmetry of the electrolyte on the low-and high-frequency relaxations. The Journal of Physical Chemistry. 1988 Jun;92(13):3905-10.

[28] Grosse C, Foster KR. Permittivity of a suspension of charged spherical particles in electrolyte solution. Journal of Physical Chemistry. 1987 May;91(11):3073-6.

[29] Grosse C, Schwan HP. Cellular membrane potentials induced by alternating fields. Biophysical journal. 1992 Dec 1;63(6):1632-42.

[30] Grosse C, Tirado M, Pieper W, Pottel R. Broad frequency range study of the dielectric properties of suspensions of colloidal polystyrene particles in aqueous electrolyte solutions. Journal of colloid and interface science. 1998 Sep 1;205(1):26-41.

[31] Han Y, Misra S. Joint petrophysical inversion of multifrequency conductivity and permittivity logs derived from subsurface galvanic, induction, propagation, and dielectric dispersion measurements. Geophysics. 2018 Apr 6;83(3):D97-112.

[32] Han Y, Misra S, Wang H, Toumelin E. Hydrocarbon saturation in a Lower-Paleozoic organic-rich shale gas formation based on Markov-chain Monte Carlo stochastic inversion of broadband electromagnetic dispersion logs. Fuel. 2019 May 1;243:645-58.

[33] Hogg AJ. Fluid Dynamics Separable solutions to Laplace’s equation. 2001.

[34] Hou CY, Feng L, Seleznev N, Freed DE. Low frequency complex dielectric (conductivity) response of dilute clay suspensions: Modeling and experiments. Journal of colloid and interface science. 2018 Sep 1;525:62-75.

[35] Jin Y, Misra S, Homan D, Rasmus J, Revil A. Mechanistic Model of Multi-Frequency Complex Conductivity of Porous Media Containing Water-Wet Nonconductive and Conductive Particles at Various Water Saturations. Advances in Water Resources. 2019 Aug 1;130:244-57.

[36] Kozbial A, Li Z, Sun J, Gong X, Zhou F, Wang Y, Xu H, Liu H, Li L. Understanding the intrinsic water wettability of graphite. Carbon. 2014 Aug 1;74:218-25.

[37] Kralchevsky PA, Eriksson JC, Ljunggren S. Theory of curved interfaces and membranes: mechanical and thermodynamical approaches. Advances in colloid and interface science. 1994 Apr 15;48:19-59.

[38] Leroy P, Revil A. A triple-layer model of the surface electrochemical properties of clay minerals. Journal of Colloid and Interface Science. 2004 Feb 15;270(2):371-80.

[39] MacLennan K, Karaoulis M, Revil A. Complex conductivity tomography using low-frequency crosswell electromagnetic data. Geophysics. 2013 Nov 22;79(1):E23-38.

[40] Martinez A, Brynes AP. Modeling dielectric-constant values of geologic materials: An aid to ground-penetrating radar data collection and interpretation. Lawrence, Kansas: Kansas Geological Survey; 2001 Dec.

[41] Misra S, Torres-Verdín C, Revil A, Rasmus J, Homan D. Interfacial polarization of disseminated conductive minerals in absence of redox-active species—Part 2: Effective electrical conductivity and dielectric permittivityInterfacial polarization due to inclusions. Geophysics. 2016a Mar 1;81(2):E159-76.

[42] Misra S, Torres-Verdín C, Revil A, Rasmus J, Homan D. Interfacial polarization of disseminated conductive minerals in absence of redox-active species—Part 1: Mechanistic model and validation. Geophysics. 2016b Mar 1;81(2):E139-57.

[43] Moss AK, Jing XD, Archer JS. Wettability of reservoir rock and fluid systems from complex resistivity measurements. Journal of Petroleum Science and Engineering. 2002 Apr 1;33(1-3):75-85.

[44] Nguyen BL, Bruining J, Slob EC. Effects of wettability on dielectric properties of porous media. In SPE Annual Technical Conference and Exhibition 1999 Jan 1. Society of Petroleum Engineers.

[45] Placencia-Gómez E, Slater LD. Electrochemical spectral induced polarization modeling of artificial sulfide-sand mixtures. Geophysics. 2014 Sep 23;79(6):EN91-106.

[46] Revil A. Effective conductivity and permittivity of unsaturated porous materials in the frequency range 1 mHz–1GHz. Water Resources Research. 2013 Jan;49(1):306-27.

[47] Revil A. Spectral induced polarization of shaly sands: Influence of the electrical double layer. Water Resources Research. 2012 Feb 1;48(2).

[48] Revil A, Abdel Aal GZ, Atekwana EA, Mao D, Florsch N. Induced polarization response of porous media with metallic particles—Part 2: Comparison with a broad database of experimental data. Geophysics. 2015 Aug 12;80(5):D539-52.

[49] Revil A, Florsch N, Mao D. Induced polarization response of porous media with metallic particles—Part 1: A theory for disseminated semiconductors. Geophysics. 2015 Aug 3;80(5):D525-38.

[50] Revil A, Murugesu M, Prasad M, Le Breton M. Alteration of volcanic rocks: A new non-intrusive indicator based on induced polarization measurements. Journal of Volcanology and Geothermal Research. 2017 Jul 15;341:351-62.

[51] Revil A, Schmutz M, Batzle ML. Influence of oil wettability upon spectral induced polarization of oil-bearing sands. Geophysics. 2011 Sep;76(5):A31-6.

[52] Schmuck M, Bazant MZ. Homogenization of the Poisson--Nernst--Planck equations for ion transport in charged porous media. SIAM Journal on Applied Mathematics. 2015 Jun 30;75(3):1369-401.

[53] Schwan HP, Schwarz G, Maczuk J, Pauly H. On the low-frequency dielectric dispersion of colloidal particles in electrolyte solution1. The Journal of Physical Chemistry. 1962 Dec;66(12):2626-35.

[54] Schwarz G. A theory of the low-frequency dielectric dispersion of colloidal particles in electrolyte solution1, 2. The Journal of Physical Chemistry. 1962 Dec;66(12):2636-42.

[55] Sihvola A. Dielectric polarization and particle shape effects. Journal of Nanomaterials. 2007 Jan 1;2007(1):5-.

[56] Spötl C, Houseknecht DW, Jaques RC. Kerogen maturation and incipient graphitization of hydrocarbon source rocks in the Arkoma Basin, Oklahoma and Arkansas: a combined petrographic and Raman spectrometric study. Organic Geochemistry. 1998 Jun 1;28(9-10):535-42.

[57] Tirado M, Grosse C. Dependence of the broad frequency dielectric spectra of colloidal polystyrene particle suspensions on the difference between the counterion and co-ion diffusion coefficients. Journal of colloid and interface science. 2006 Jun 15;298(2):973-81.

[58] Tissot BP, Welte DH. Petroleum formation and occurrence. Springer Science & Business Media; 2013 Nov 11.

[59] Tuncer E, Gubański SM, Nettelblad B. Dielectric relaxation in dielectric mixtures: Application of the finite element method and its comparison with dielectric mixture formulas. Journal of Applied Physics. 2001 Jun 15;89(12):8092-100.

[60] Ujiié Y. Kerogen maturation and petroleum genesis. Nature. 1978 Mar;272(5652):438.

[61] Weisstein EW. Legendre polynomial. http://mathworld.wolfram.com/LegendrePolynomial.html; 2018a, accessed Nov 11 2018

[62] Weisstein EW. Bessel function. http://mathworld.wolfram.com/BesselFunction.html; 2018b, accessed Nov 11 2018

[63] Winchell AN. A theory for the origin of graphite as exemplified in the graphite deposit near Dillon, Montana. Economic Geology. 1911 Apr 1;6(3):218-30.

[64] Wong J. An electrochemical model of the induced-polarization phenomenon in disseminated sulfide ores. Geophysics. 1979 Jul;44(7):1245-65.

[65] Young P. Helmholtz’s and laplace’s equations in spherical polar coordinates: Spherical harmonics and spherical bessel functions. Physics 116C Lecture Notes, University of California, Santa Cruz, CA. http://physics. ucsc. edu/~ peter C. 2009;116.

[66] Zheng Q, Wei GW. Poisson–Boltzmann–Nernst–Planck model. The Journal of chemical physics. 2011 May 21;134(19):194101.